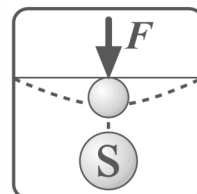


**Sergey Y. Yurish**  
Editor

**Sensors, Measurements  
and Sensor Systems**



## Sensors, Measurements and Sensor Systems



Sergey Y. Yurish  
Editor

# **Sensors, Measurements and Sensor Systems**

**Book Series: Advances in Sensors, Vol. 9**



International Frequency Sensor Association Publishing

Sergey Y. Yurish  
*Editor*

Sensors, Measurements and Sensor Systems  
Advances in Sensors, Vol. 9

Copyright © 2025 by International Frequency Sensor Association Publishing, S. L.

E-mail (for orders and customer service enquires): [ifsa.books@sensorsportal.com](mailto:ifsa.books@sensorsportal.com)

Visit our Home Page on <http://www.sensorsportal.com>

All rights reserved. This work may not be translated or copied in whole or in part without the written permission of the publisher (IFSA Publishing, S. L., Barcelona, Spain).

Neither the authors nor International Frequency Sensor Association Publishing accept any responsibility or liability for loss or damage occasioned to any person or property through using the material, instructions, methods or ideas contained herein, or acting or refraining from acting as a result of such use.

The use in this publication of trade names, trademarks, service marks, and similar terms, even if they are not identifying as such, is not to be taken as an expression of opinion as to whether or not they are subject to proprietary rights.

ISBN: 978-84-09-57646-3  
BN-20250520-XX  
BIC: TJFC

## Acknowledgments

As Editor I would like to express my undying gratitude to all authors, editorial staff, reviewers and others who actively participated in this book. We want also to express our gratitude to all their families, friends and colleagues for their help and understanding.



# Contents

<b>Contributors.....</b>	<b>9</b>
<b>Preface .....</b>	<b>11</b>
<b>1. Underwater 3D Sensor System for Mobile Mapping .....</b>	<b>13</b>
1.1. Introduction.....	13
1.2. The Underwater 3D Sensor System.....	15
1.2.1. Hardware Setup .....	15
1.2.2. User Interface .....	16
1.3. Data Processing for Mobile Mapping.....	17
1.3.1. Calibration and 3D Calculation .....	17
1.3.2. Visual and Inertial Odometry .....	18
1.3.3. Motion Compensation .....	19
1.3.4. Registration of the Point Clouds.....	20
1.3.5. Generation of 3D Color Models .....	21
1.4. Results .....	22
1.5. Conclusion and Outlook.....	24
Acknowledgements .....	25
References .....	25
<b>2. Torsion Energy to Control an Electromagnetic Plasma in a Reactor: Analysis in DC-regime and Fermionic Flow Derivations .....</b>	<b>27</b>
2.1. Introduction.....	27
2.2. Electronics Experiments to Design of a Device Control.....	29
2.3. Derived Fermionic Products.....	31
2.4. Conclusions.....	36
Technical Notation.....	37
References .....	37
<b>3. A Low-cost and Flexible Prototype for Static and Dynamic Calibration of Pressure Measurement Channels .....</b>	<b>39</b>
3.1. Introduction.....	39
3.2. Calibration.....	40
3.2.1. Static Calibration.....	41
3.2.2. Dynamic Calibration.....	41
3.3 Pressure Measurement Channel .....	43
3.4. Calibration Prototype .....	44
3.4.1. Hardware .....	45
3.4.2. Software.....	46
3.5. Experimental Results.....	47
3.5.1. Industrial Pressure Transmitter.....	48
3.5.2. Non-invasive Automatic Blood-pressure Sphygmomanometer.....	51
3.6. Conclusions.....	54
Acknowledgements.....	54
References .....	54





# Contributors

**Michael Bleier**

Fraunhofer Institute for Applied Optics and Precision Engineering IOF, Jena, Germany

**Christian Bräuer-Burchardt**

Fraunhofer Institute for Applied Optics and Precision Engineering IOF, Jena, Germany

**Francisco Bulnes**

IINAMEI, Research Department in Mathematics and Engineering, GI-TESCHA, México

**J. C. García-Limón**

IINAMEI, Research Department in Mathematics and Engineering, GI-TESCHA, México

**Artur M. F. Graxinha**

Instituto Politécnico de Setúbal, ESTSetúbal, Campus do IPS, Estefanilha, Edifício Sede, 2910-761 Setúbal, Portugal

**Peter Kühmstedt**

Fraunhofer Institute for Applied Optics and Precision Engineering IOF, Jena, Germany

**Christoph Munkelt**

Fraunhofer Institute for Applied Optics and Precision Engineering IOF, Jena, Germany

**Gunther Notni**

Fraunhofer Institute for Applied Optics and Precision Engineering IOF, Jena, Germany

**José Dias Pereira**

Polytechnic Institute of Setúbal, ESTSetúbal, Campus do IPS, Estefanilha, Edifício Sede, 2910-761 Setúbal, Portugal

Telecommunications Institute, Lisbon, Portugal

**Octavian Postolache**

Instituto de Telecomunicações IT-IUL, Instituto Universitário de Lisboa, ISCTE-IUL, Lisboa, Portugal

**Victor Sánchez**

IINAMEI, Research Department in Mathematics and Engineering, GI-TESCHA, México

**Vítor Viegas**

CINAV – Escola Naval, Base Naval de Lisboa, Almada, Portugal



# Preface

The 9<sup>th</sup> volume of the ‘*Advances in Sensors*’ Book Series—Sensors, Measurements and Sensor Systems—is presented as a resource for academics engaged in the research, development, and application of advanced sensor technologies. This volume is designed to serve as both a reference and a stimulus for inquiry among university professors, doctoral students, and postdoctoral researchers working across electrical engineering, applied physics, mechatronics, and instrumentation science.

Sensor systems are foundational to modern scientific investigation and technological development. As instrumentation continues to evolve toward higher precision, integration, and intelligence, academic research plays a crucial role in shaping the principles, models, and architectures that define next-generation sensing platforms. This volume brings together substantive chapters, each offering a rigorous contribution grounded in experimental validation and/or theoretical modeling.

**Chapter 1** presents a comprehensive exploration of a mobile optical sensing solution for underwater environments. Developed through collaboration between research institutions and industry partners, the system integrates structured light projection, stereo vision, inertial sensing, and real-time 3D reconstruction algorithms. With a focus on accuracy, robustness, and operability in dynamic offshore conditions, this work addresses key challenges in subsea inspection, archaeological documentation, and marine ecology monitoring. The chapter is rich in methodological detail, including calibration strategies, visual-inertial odometry techniques, SLAM-based 3D registration, and hardware-software integration, making it particularly relevant for graduate-level research in robotics, computer vision, and sensor fusion.

**Chapter 2** ventures into the intersection of electromagnetic field theory, plasma dynamics, and topological modeling. The authors propose an innovative framework for controlling plasma behavior through magnetic curvature energy, supported by electronic circuit implementations and derived mathematical formulations. Their analysis extends to the behavior of fermionic products and potential applications in propulsion systems, offering conceptual depth for theoretical physicists and engineering researchers interested in magnetohydrodynamics, plasma electronics, and emerging energy systems. The chapter will appeal to doctoral researchers seeking novel applications of topological field theory in physical systems.

**Chapter 3** addresses the need for accessible and accurate pressure calibration methods in both industrial and biomedical domains. The authors detail the design and testing of an electro-pneumatic calibration platform that supports time- and frequency-domain assessments of pressure transducers. Of particular relevance is the system's capability to account for the dynamics of capillary lines and sensing volumes—factors often overlooked in field deployments. The chapter includes practical insights into sensor modeling, system identification, and LabVIEW-based software development, offering a

valuable case study for coursework or research in measurement systems, control engineering, and experimental instrumentation.

In compiling this volume, our goal is to offer a resource that is both technically robust and pedagogically valuable. Each chapter has been peer-reviewed and selected for its potential to advance the state of knowledge, support research training, and foster interdisciplinary dialogue. I encourage faculty members to consider the content herein for advanced seminar discussions, while PhD students may find useful frameworks and experimental models to build upon in their own theses and dissertations.

I extend my sincere appreciation to the authors for their scholarly contributions and to the reviewers and editorial collaborators for their careful evaluations and recommendations. This volume would not have been possible without their dedication to scientific rigor and academic excellence.

*Dr. Sergey Y. Yurish*  
*Editor*  
*IFSA Publishing*

*Barcelona, Spain*

# **Chapter 1**

## **Underwater 3D Sensor System for Mobile Mapping**

**Christian Bräuer-Burchardt, Michael Bleier, Christoph Munkelt, Peter Kühmstedt, and Gunther Notni**

### **1.1. Introduction**

Accurate 3D measurements of underwater objects are of increasing interest to archaeologists, marine scientific researchers such as biologists or geologists, and energy enterprises. Examples of industrial applications of underwater 3D measurement tasks are inspections of oil or gas pipelines, offshore windpark foundations, and anchor chains [1]. Archaeologists and cultural heritage conservationists are interested in submerged site documentation [2, 3], shipwreck 3D reconstruction [4, 5], or cave exploration [6], including 3D mapping. Biologists document the growth of the seabed, observe the state and the temporal development of coral reefs [7], or determine the size of certain fish species [8]. Geologists use measurement data for modeling the transportation of sediments. Offshore structures, such as wind turbine foundations or oil platforms, need regular inspections and maintenance to check dimensions, identify small damages, or monitor the appearance of corrosion.

Devices and components which should be inserted into offshore structures must often be constructed very precisely onshore. The required dimensions must be observed offshore with the highest accuracy as a prerequisite. Especially connection and fitting pieces for pipelines must be produced very accurately because connections must not leak despite temperature and pressure changes of the transported gases or liquids. Hence, exact 3D measurements are necessary.

The measurement accuracy for the positioning of connection parts of pipelines must be within a few centimeters and angle errors must be below half a degree per 100 m distance. For industrial applications, this is typically achieved by marker-based photogrammetry.

However, additional infrastructure is necessary in terms of optical markers which must be fixed on the seabed.

Other common techniques for underwater 3D reconstruction besides photogrammetry (see, e. g., [9]) are laser scanning [1, 10], sonar-based seabed mapping [11, 12], and time-of-flight methods [13]. Recent developments include structure from motion (SfM) [14] or provide systems based on video streams that allow capturing data for 3D reconstruction in motion [15]. A plenoptic camera solution is provided by Skinner [16]. A novel commercial photogrammetric underwater scanner is offered by Vaarst [17] which also processes video streams.

Several partners from industry and research developed a novel optical underwater 3D sensor system for mobile offshore 3D measurement of industrial structures and other objects of interest in a funded project. The sensor system is conceived to be mounted to a remotely operated vehicle (ROV). The sensor system is shown in Fig. 1.1, mounted on a hydraulic manipulator arm of a ROV. The sensor system permanently scans the environment at a certain distance and field of view and generates up to 50 single scans per second, which are merged into a common 3D model in real-time. The sensor system can be propelled with a velocity of up to 1 m/s.



**Fig. 1.1.** Sensor system mounted on a work-class ROV.

The novel system has the following features:

- Surface-based recording with a measurement volume of about  $0.9 \text{ m} \times 0.8 \text{ m} \times 0.8 \text{ m}$  at a mean scanning distance of 2 m for a single scan;
- Very small systematic measurement error of below 1 mm in the complete measurement volume;
- High density of 3D points (one million 3D points per scan), high 3D scan rate of 50 Hz;

- Simultaneous recording of 3D points and high-resolution color images using an LED flash;
- Automatic motion compensation based on visual and inertial odometry [18] during image recording;
- Graphical user interface including real-time visualization for quality check and support of the ROV pilot during image recording.

## **1.2. The Underwater 3D Sensor System**

The main part of the sensor system is a structured illumination based stereo sensor. The projection unit uses the GoBo technique [19] for production of aperiodic sinusoidal fringe patterns. A powerful LED is used as the light source and the geometry of the GoBo wheel is specifically designed to obtain maximum contrast and suitability for the desired frame rates. The rotation velocity of the wheel is also optimized according to the selected image recording frame rate.

The generation of highly resolved 3D data is based on stereo triangulation and correspondence-finding according to temporal gray value sequence correlation. The sequence length is usually ten images and up to 900 fps 2D image frame rate is used. The stereo sensor continuously captures 3D data at a typical distance of two meters with a field of view of approximately one square meter. The strongly overlapping 3D point clouds are merged to a common 3D model of the observed objects. Simultaneously, 2D color images with a resolution of 7 MPix are recorded with 25 fps covering a field of view at two meters distance of about  $2 \text{ m} \times 2 \text{ m}$ . The control unit of the system triggers the recordings in an alternating manner. The color camera capturing is synchronized with a flash for optimal illumination while LED illumination of the structured light pattern is switched off during the color camera exposure. To minimize the disruptive effect of the flashlight on the structured illumination, there are short periods of time without exposure between the recordings of the color and monochrome cameras.

### **1.2.1. Hardware Setup**

The main components of the sensor system are built into five underwater housings making the system applicable to depths up to 1000 meters (see Fig. 1.2). The outer two housings contain the two monochrome measurement cameras. One housing includes the projection unit consisting of an LED light source emitting blue light, a rotation wheel contains the aperiodic sinusoidal fringe pattern, a wheel motor, and the projection lens. The same housing contains electronic drivers and a control unit. The fourth housing contains the color camera and an inertial measurement unit (IMU) with a fiber-optic gyroscope.

All four housings are fixed on a bar of carbon fiber which is vibrationally decoupled from the carrier frame. This ensures a high calibration stability of the sensor system. Additionally, two LED flash units are mounted on the sides of the sensor carrier to illuminate the measurement object but prevent illumination of particles in the near range to avoid scattering effects.



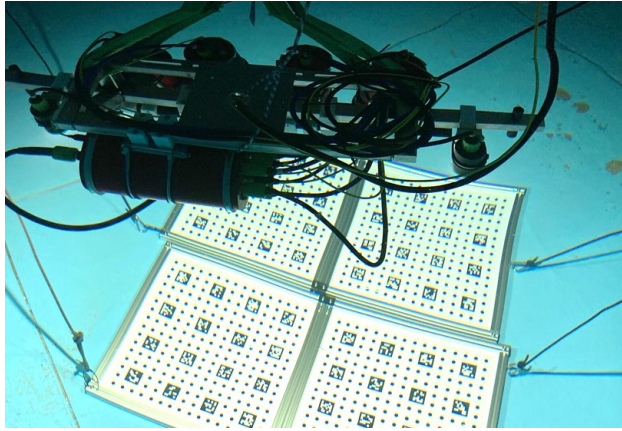


**Fig. 1.2.** Sensor system at calibration using marker boards in a water basin.

A fifth housing, which does not need certain geometric adjustment to the other housings, contains the electronics for power supply and the network technology for data transfer.

All data are transferred via a network using the glass fiber tether of the ROV. The 3D calculation and data analysis are performed above water on the vessel using a PC workstation which is directly connected to the sensor system by a ten-gigabit glass fiber cable. Hence, it is not necessary to add another underwater housing containing powerful hardware for calculation tasks, which would mean more weight and costs. 3D reconstruction and model generation are performed online to ensure a direct quality check of the recordings.

### 1.2.2. User Interface

A key factor in the effective use of the sensor for measurement applications is the user interface. To this end, software was developed by our project partner 3++ [20]. This software provides a visualization for the ROV pilot as well as the interface for the operator of the sensor system. An example is shown in Fig. 1.3.

The software performs the parameter setting of the sensors to quickly adapt exposure time and light sensitivity to the environmental conditions in the water. The software aids in recognition of faulty exposures in certain regions of the images and directly shows the 3D reconstruction result for a quality check. Additionally, the user interface allows control the datastream recording as well as the triggering of single shots, e. g., as part of the calibration procedure.

A display of the stream of color images is provided to the ROV pilot with short latency to support the navigation task. The monitor provides various optical aids to help the ROV pilot achieve the optimal distance between the sensor and the measurement object. A visualization of the 3D data, which is more difficult to interpret than color images, is not necessary for the ROV pilot.

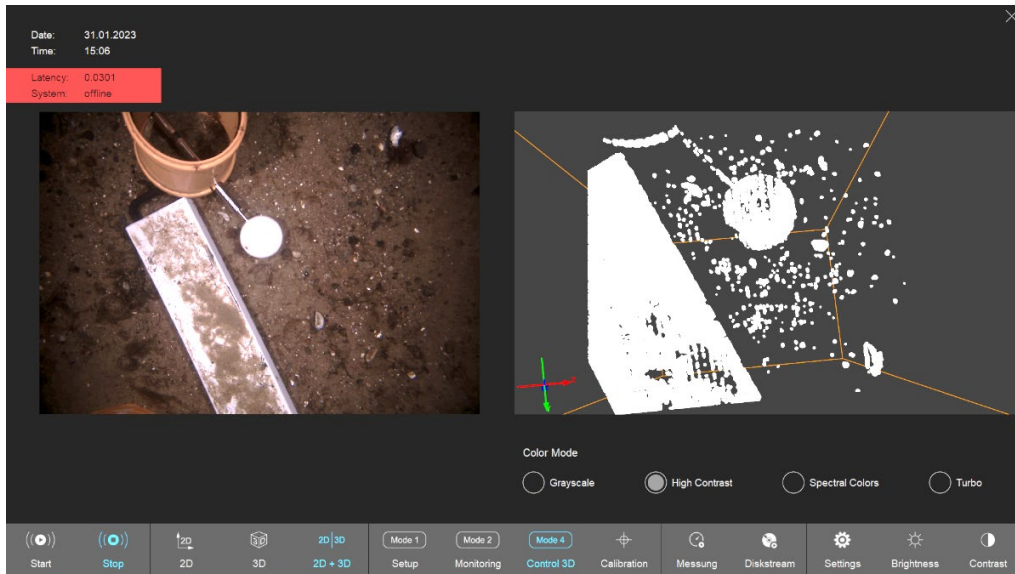


**Fig. 1.3.** User interface of the monitoring software.

For visualization of the complete 3D model a browser-based solution using Potrees [21] was developed. This includes user management, organization in scan projects, and automated generation of previews of the point clouds. Web technology was chosen to enable remote access and 3D data observation without special 3D software tools. This means that all interested parties can observe and analyse the data independently. Furthermore, it enables data transfer via cellular network or a satellite link between the location of measurement and an office location. This promotes parallel data analysis and may reduce the personnel effort on the vessel during the measurement procedure.

### 1.3. Data Processing for Mobile Mapping

The system performs a motion estimation and a fusion into a complete and coherent 3D model. The motion of the sensor is estimated using visual odometry [18] in combination with a fiber optical gyroscope. The quickly derived poses are provided to the system to realize real-time motion compensation of the 3D scans. Subsequently, a multiple-step registration strategy is applied to achieve a further refinement of the trajectory estimation. According to the determined sensor trajectory, single scans are merged into a global 3D model and visualized with reduced resolution. Hereby, quality checks are even possible during the data recording.

#### 1.3.1. Calibration and 3D Calculation

Recordings of the two monochrome measurement cameras illuminated by the GoBo-based projection unit are used to establish the 3D measurement. 3D data are obtained by triangulation of corresponding points of the calibrated cameras.

Correspondence-finding is realized by temporal correlation of the gray value sequences with a length of ten images (see [19]).

For underwater use, an extended pinhole camera model is applied which takes refraction at the interfaces between air and glass and glass and water into account [20]. Locally dependent scaling errors are detected by a specific arrangement of ball-bar measurements and compensated by a correction function in the measurement volume [23].

Calibration is performed using a pattern of markers in a specific arrangement, including circles and ArUco markers (see Fig. 1.2). The calibration pattern is fixed on the floor of a water basin or on the seafloor, and the sensor takes images from ten to twenty different positions in slow movement with all three cameras. The calculation of the set of calibration parameters is performed as stereo camera calibration using the commercially available bundle adjustment software BINGO [24]. Stereo calibration is performed both between the two monochrome measurement cameras and between the left camera and the color camera. The left camera provides the reference co-ordinate system for the 3D measurement. Both stereo calibrations are performed at the same time, with identical input data.

### 1.3.2. Visual and Inertial Odometry

The principle of visual odometry [18] is applied to obtain a real-time estimation of the trajectory of the sensor system using the IMU. This occurs independently from 3D data calculation. The technique is based on VINS-Mono [25] using the Harris feature detector (also known as the Shi-Tomasi method) for automatic extraction of image features for visual odometry.

First, pose estimation must be initialized. This means that the method can be used only after some three seconds of motion. The sensor must be moved for generation of enough parallax for an initial unscaled structure-from-motion reconstruction (SfM) of the feature points. The scaling is realized using the recorded IMU data. After finishing initialization, the process of measurement can start.

The relative orientation between the color camera and the IMU is determined in air. The parameters of the camera-IMU-transformation are fixed for underwater use. Typically, no rotations around all sensor axes are produced under water because of the characteristic ROV movements. Hence, translation between camera and IMU is inaccurately estimated. A fast initialization of visual odometry is also possible for approximately linear trajectories if the camera-IMU-transformation is considered as known. The stochastic error parameters were determined using the function graph of the Allan variance [26] of the IMU data stream over several hours. However, this was not used for a complete model of noise behavior and measurement uncertainty but for estimation of weights of camera vs. IMU based motion estimation.

The time delay between camera recordings and IMU data is constantly estimated because no common time trigger process was implemented. The relative movement is calculated

by equalization of the visual and the IMU data in a local environment. Optimization is performed over a consecutive group of keyframes which are selected based on a threshold applied to the average parallax of the feature points. It should be noted that this step does not contain re-localization or closing of loops according to visual features. The goal is to obtain a continuous trajectory without jumps, because visual odometry should also be used for local motion compensation. A possible drift caused by remaining errors will be corrected later within the 3D registration process.

### 1.3.3. Motion Compensation

As previously described, 3D calculation is based on temporal correlation over a stack of gray value images of the left and the right measurement camera. This approach is typically used for static scenes. However, this precondition is not fulfilled in the case of a moving sensor, as a permanent start-and-stop regime is not meaningful or feasible. A quasi-static measurement situation is not realistically achievable, because this requires ultrafast pattern projection and recording with exposure times below 0.2 milliseconds. Due to light absorption, turbidity, and limited illumination power, this is not possible under water with the current state of technical development of the equipment.

Consequently, the approach for the 3D sensor system is to compensate disruptive motion effects algorithmically. A detailed description of this approach is described in [23] and [27]. The correction algorithm changes the content of the recorded images according to the estimated velocity of the sensor and the distance of the object. For the time of sequence recoding (ten images) a constant velocity is assumed. Using the motion estimation by visual odometry and an assumed average object distance, a sub-pixel-accurate shift of every image of the sequence is performed. The calculated translation is applied before correspondence search.

If motion correction is applied a considerable improvement of the measurement results is achieved. This improvement means a more complete 3D point cloud as well as an increased measurement accuracy. Typically, more 3D points can be reconstructed due to a reduction of image artifacts. Fig. 1.4 shows an example of a successful application of the motion correction to a measurement taken at 0.7 m/s velocity of the sensor. The left image shows 3D reconstruction result without, the middle one with manual, and the right with automatic motion compensation. A significant improvement of the result is visible.

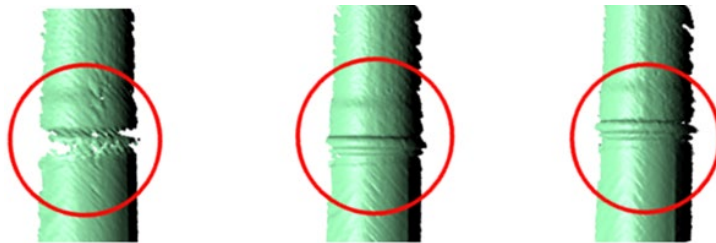


**Fig. 1.4.** Motion compensation example: without (left), manually corrected (middle), and automatically corrected (right) 3D dataset of a pipe segment.

### 1.3.4. Registration of the Point Clouds

The initial estimation of the trajectory by visual odometry is extended by a multiple-step registration strategy to achieve a further refinement. Fig. 1.5 shows an overview of the processing steps. The first two stages are carried out at the same time as the data is recorded and allow the operator to make an initial assessment of the results. A global optimization of the 3D point cloud is made in a post-processing step.

#### Online registration

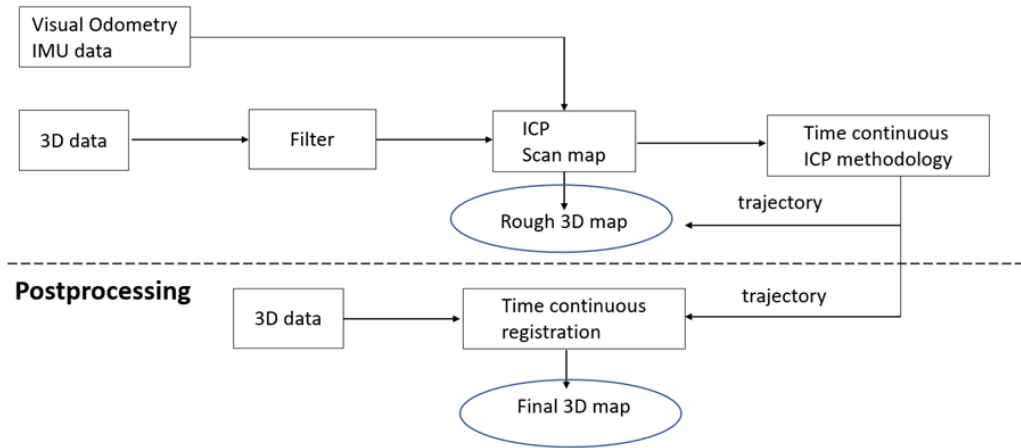


**Fig. 1.5.** Overview of registration process.

In preparation for registration, the 3D points are filtered to reduce the size of the point cloud to be processed. Additionally, a balanced spatial distribution of the selected points should be achieved. Using the Iterative Closest Point (ICP) algorithm, each 3D point cloud is sequentially registered against its predecessors with the goal of local optimization of the trajectory and improvement of the resulting 3D map. For this a metascan created from a sliding window of registered preceding scans is used to provide more structure during ICP registration. A metascan size that corresponds to the number of scans captured in the previous 3s is selected. The search radius is set quite small (only few centimeters) depending on the velocity of the sensor to reduce the risk of rough registration errors because of the limited field of vision and the expected weak geometric structure of the scene.

Sufficient 3D structure in the point cloud is necessary for convergence of the ICP registration and hence for a successful 3D scan. However, depending on the recorded measurement scene, this is not always the case. If, for example, only the cylindrical surface of a pipe is recorded, then the registration in the direction of the pipe is uncertain. In these cases, the ICP registration is deactivated and only the trajectory estimation of the visual odometry is used in this initial step.

Since the remaining errors accumulate in the registration and the existing drift of the visual odometry is not eliminated, the next step is a second registration using a continuous ICP technique. The key concept is that the error of the trajectory in temporal proximity of a considered pose. The trajectory is then split into sections and several consecutive 3D scans are combined around a selected reference scan to generate a partial map. The partial maps are again registered against their predecessors.

To maintain the continuity of the trajectory, the change in the pose of a reference scan is subsequently spread to the poses between two reference scans. A linear distribution of the translation or a distribution of the rotational errors with Spherical Linear Interpolation (SLERP) is sufficient for small changes. To correct the accumulated drift, loops are detected and closed [28]. To do this, the poses of the aggregated partial maps are optimized. Finally, the detected changes are distributed to the individual poses in the same manner.

The resulting map is used for visualization during the measurement process. To reduce the data size for visualization, the individual scans are thinned out. For this purpose, a new scan is only added to the overall model, when the sensor system has moved at least five to ten centimeters, depending on the desired point density. The spatial resolution of the 3D map generated from the aggregated individual scans based on the determined trajectory is subsequently reduced in an octree-based process and made available for visualization. This happens asynchronously to the trajectory estimation and registration. Every one to five seconds the 3D model is updated and made available for visualization.

Post-processing of the data to generate the final 3D point cloud is achieved using continuous-time SLAM [29]. In this step the subsections of the trajectory are created in a way that they partially share scans with the previous and next partial map to ensure sufficient overlap for registration. After applying a globally consistent scan matching a semi-rigid matching is applied for the numerical minimization of the trajectory error.

### **1.3.5. Generation of 3D Color Models**

Besides the motion compensation of the 3D scans, the trajectory estimation is an essential requirement for the precise coloring of the point clouds. Since the color images are recorded with a time delay between the stereo images of the monochrome measurement cameras, there is a time difference of up to 10 ms between the 3D scan and the next color image. Hence, the motion of the sensor must be considered to correctly project the color information onto the point cloud. This is done as follows: first, the trajectory calculated from visual odometry is interpolated to calculate the relative motion of the camera between the acquisition time of the 3D scan and the color image. The time stamp of the sensor control is used for this.

Subsequently, the point cloud is merged with the pixel values of the color camera using the co-calibration of color camera and stereo sensor and the estimated sensor motion. Finally, the whole point is colored by projection of the color pixel onto the 3D model.

## **1.4. Results**

During the sensor development, various tests were carried out under water. In addition to the sample 3D recording of certain test objects, an accuracy determination was carried out using ball-bars and standardized flat objects. Random and systematic measurement errors were estimated.

Initially, these tests were carried out in water basins to keep the logistical effort as low as possible and to enable precise control of certain influences such as water quality, measurement distance and sensor speed. After successfully completing the water basin tests, the sensor system was applied offshore in the Baltic Sea mounted on a remotely operated vehicle (ROV). During the tests in the water basin, the sensor was set and calibrated for a mean measurement distance of 2.0 meters, and for offshore use for an average measurement distance of 1.3 meters.

In the first experiments the water basin was filled with clear fresh water. The first experiment comprised the determination of systematic and random measurement 3D errors of a single scan. Based on the VDI/VDE standard 2634 [30], length measurement and flatness errors as well as the noise in the 3D measurement points were determined as a function of the measurement distance. The sensor was mounted on a crane and was well-placed in relation to the desired position of the test measurement objects (ball bar, flatness object). The detailed results are documented in [23]. A slight drift of 0.08 % was detected in the ball diameter and measurements of the sphere-to-sphere distance proportional to the object distance. This error was minimized with a 3D correction function. The flatness error increased with large distances to the object [23]. Due to the small number of measurements a valuable correction function could not be determined. However, due to the expected deviations of the real mapping from the extended pinhole camera model [31], the distance-dependent error corresponding with the relatively large depth variation is in the expected range.

Due to the mounting on the Remotely Operated Vehicle (ROV) and the significantly reduced visibility compared to the water basin, no exact distances to the measurement objects could be determined for the measurements in the sea water. The measurement objects were scanned by the sensor system in motion. A distance-dependent accuracy study was carried out using the mean object distance. Object distance was determined retrospectively using the absolute 3D object co-ordinates of the scans. Measurement values were determined in the range of approximately 1.1 to 1.6 meters distance. Here, a distance-dependent drift of 0.4 % was observed in the measurements. This drift, however, was not observed in the determination of the diameter of the spheres. Possible reasons are systematic errors in determination of the radius of the spheres. The random length measurement error in repeated measurements at the same measurement distance increased by a factor two compared to the water basin measurements. However, this value is not significant because too few measurements were captured, and it is not sure that external conditions were constant. Selected measurement values are summarized in Table 1.1. The calibrated length of the sphere-to-sphere distance of the ball-bar is 497.612 mm. A slight scaling error of less than one percent also occurred with the second sensor.

**Table 1.1.** Random Length measurement error at water basin measurements (using sensor system 1) and offshore (sensor system 2). Calibrated length of ball-bar is 497.612 mm.

System 1	Location: water basin		System 2	Location: Baltic Sea	
Distance [m]	measurement sphere distance [mm]	n	Distance [m]	measurement sphere distance [mm]	n
$1.54 \pm 0.00$	$497.602 \pm 0.030$	6	$1.16 \pm 0.02$	$499.655 \pm 0.105$	10
$1.94 \pm 0.01$	$497.873 \pm 0.040$	6	$1.28 \pm 0.01$	$500.067 \pm 0.186$	10
$2.24 \pm 0.00$	$498.144 \pm 0.037$	5	$1.57 \pm 0.03$	$501.716 \pm 0.167$	10

A significant flatness error was registered at distances below 1.2 m, whereas at longer distances no typical warping effect occurred. Due to the small number of measurements at different distances, determination of a correction function was not possible.

In summary, it was determined that the random measurement error at offshore conditions compared to the water basin increased by a factor two. This was observed both at the repeated length measurements of the ball-bar and the noise of the measured 3D points. The systematic measurement error was significantly higher in the offshore measurements than in the water basin. This may be caused by a less good calibration, which could not be repeated and optimized due to a lack of resources.

In addition to the measurements of the calibrated test bodies, the sensor system was validated for the mobile recording of pipe structures. Further measurement objects were a dummy bomb and terracotta jars. See Fig. 1.6 below for an example of a point cloud recorded in motion during measurements in the Baltic Sea. The red line visualizes the trajectory estimated by the system in real-time.

To verify the trajectory determination using visual and inertial odometry, ball-bars were installed on the seabed. The spheres on a bar are 10 cm in diameter and spaced 2.2 m apart. The ball-bars were scanned with the ROV-mounted underwater sensor. Fig. 1.7 shows the composite point cloud from 3D scans taken in motion.

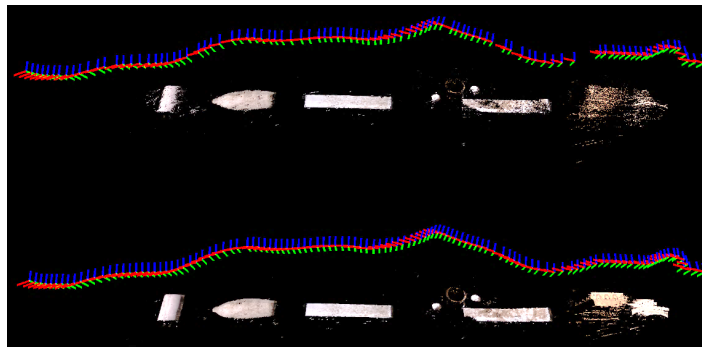


**Fig. 1.6.** Measurement example with color mapping without (above) and with motion compensation (below). Red line shows the determined trajectory.



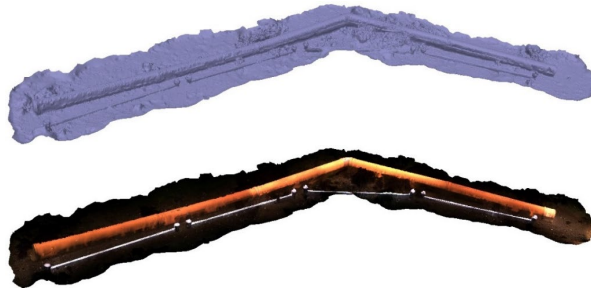


**Fig. 1.7.** Measurement example of a pipeline segment and ball-bars for scaling determination: 3D surface representation (above) and color mapped model (below).

The mean measured ball spacing is  $2.212 \pm 0.011$  m. The mean absolute deviation of the ball spacing is 8 mm. In this case, it was not possible to improve the result by registering the 3D data because the scans did not contain enough 3D structure. Due to the high reflectivity of the spheres and metal profiles, the sea floor and the ball-bars could not be captured simultaneously in one scan.

## 1.5. Conclusion and Outlook

The newly developed sensor system demonstrated mobile detection of structures both in clear water and in experiments mounted to an underwater vehicle in the Baltic Sea. The 3D reconstruction based on active stereo with illumination of structured light allows a two-dimensional acquisition and a 3D sampling rate of up to 50 Hz. Particular attention is paid to the calibration procedure for the underwater stereo scanner. It is based on the geometric modeling of the vision rays, considering the refraction at the media transitions. Additional refinement procedures furthermore reduce the systematic measurement error of the sensor system.

Additionally, the system performs motion estimation and correction of disruptive motion effects as well as a fusion of the individual scans into a globally consistent 3D model. In the case of mobile measurements, an improvement of the quality of the 3D point cloud was achieved by automatic motion compensation using visual odometry.

In experiments in clear water, measurement results are achieved with a very small systematic error. These errors are in the same accuracy range as measurements in air over a comparable measurement volume. The offshore measurements showed an increase of the random length measurement error in repeated measurements at the same measurement distance compared to the water basin measurement. Furthermore, there was a slight scaling error of almost one percent. A comprehensive evaluation is still pending.

While mobile mapping was successfully demonstrated based on visual odometry, the application of 3D registration was not successful on all offshore recordings. Due to the limited field of view and measurement range, there is not always enough 3D structure to completely restrict the registration in all spatial directions. A combined process that

simultaneously aligns color and 3D information could improve the results here. The method presented uses both the color images and the 3D scans for the trajectory estimation. However, the trajectory is calculated in a sequential method. Further research is necessary to ensure highly accurate and robust registration in all situations.

## Acknowledgements

This research was funded by the German Federal Ministry for Economic Affairs and Climate Action, grant number 03SX482C. The authors like to thank the enterprises SeaRenegy Offshore Holding GmbH and Cie. KG, Oktopus GmbH, and 3++ GmbH, who were involved in the research project and took part in conception, construction, and software development for the underwater sensor system. Additionally, we like to thank Digital Ocean Lab Rostock and Baltic Diver Rostock GmbH for supporting the off-shore experiments.

## References

- [1]. D. McLeod, J. Jacobson, M. Hardy, C. Embry, Autonomous inspection using an underwater 3D LiDAR, in *Proceedings of the OCEANS Conference*, San Diego, CA, USA, 23-27 September 2013, NY, USA, pp. 1-8.
- [2]. C. A. Collin, P. Archambault, B. Long, Mapping the Shallow Water Seabed Habitat With the SHOALS, *IEEE Trans. Geosci. Remote Sensing*, Vol. 46, Issue 10, 2008; pp. 2947-2955.
- [3]. A. Georgopoulos, P. Agrafiotis, Documentation of submerged monument using improved two media techniques, in *Proceedings of the 18<sup>th</sup> International Conference on Virtual Systems and Multimedia 18th International Conference on Virtual Systems and Multimedia (VSMM'12)*, 2012, pp. 173-180.
- [4]. C. Balletti, C. Beltrane, E. Costa, F. Guerr, P. Vernier, Underwater photogrammetry and 3D reconstruction of marble cargos shipwrecks, *Int. Arch. Photogrammetry, Remote Sensing and Spatial Information Sciences*, Vol. XL-5/W5, April 2015, pp. 7-13.
- [5]. M. O. Zhukovsky, V. D. Kuznetsov, S. V. Olkhovsky, Photogrammetric techniques for 3-D underwater record of the antique time ship from Phangoria, *International Archives of the Photogrammetry, Remote Sensing and Spatial Information Sciences*, Vol. XL-5/W2, 2013, pp. 717-721.
- [6]. P. B. Campbell, An Introduction to Archaeology in Underwater Caves, *Highfield Press*, 2018, pp. 5-26.
- [7]. J. C. Bythell, P. Pan, J. Lee, Three-dimensional morphometric measurements of reef corals using underwater photogrammetry techniques, *Coral Reefs*, Vol. 20, 2001, pp. 193-199.
- [8]. C. Costa, A. Loy, S. Cataudella, D. Davis, M. Scardi, Extracting fish size using dual underwater cameras, *Aquac. Eng.*, Vol. 35, 2006, pp. 218-227.
- [9]. G. Telem, S. Filin, Photogrammetric modeling of underwater environments, *ISPRS J. Photogramm. Remote Sens.*, Vol. 65, 2010, pp. 433-444.
- [10]. C. S. Tan, G. Seet, A. Sluzek, D. M. He, A novel application of range-gated underwater laser imaging system (ULIS) in near-target turbid medium, *Opt. Lasers Eng.*, Vol. 43, 2005, pp. 995-1009.
- [11]. T. Guerneve, Y. Pettillot, Underwater 3D reconstruction using BlueView imaging sonar, in *Proceedings of the OCEANS Conference*, 2015, pp. 1-7.
- [12]. ARIS-Sonars, <http://soundmetrics.com/Products/ARIS-Sonars>
- [13]. 3DatDepth, <http://www.3datdepth.com/>

- [14]. S. Catalucci, R. Marsili, M. Moretti, G. Rossi, Point cloud processing techniques and image analysis comparisons for boat shapes measurements, *Acta IMEKO*, Vol. 7, 2018, pp. 39-44.
- [15]. C. Beall, B. J. Lawrence, V. Ila, F. Dellaert, 3D reconstruction of underwater structures, in *Proceedings of the IEEE/RSJ International Conference on Intelligent Robots and Systems (IROS'10)*, Taipei, Taiwan, 18-22 October 2010, pp. 4418-4423.
- [16]. K. A. Skinner, M. Johnson-Roberson, Towards real-time underwater 3D reconstruction with plenoptic cameras, in *Proceedings of the IEEE/RSJ International Conference on Intelligent Robots and Systems (IROS'16)*, Daejeon, Korea, 2016, pp. 2014-2021.
- [17]. Vaarst, <https://vaarst.com/subslam-3d-imaging-technology/>
- [18]. K. Yousif, A. Bab-Hadiashar, R. Hoseinnezhad, An Overview to Visual Odometry and Visual SLAM: Applications to Mobile Robotics, *Intell. Ind. Syst.*, Vol. 1, 2015, pp. 289-311.
- [19]. S. Heist, P. Dietrich, M. Landmann, P. Kühmstedt, G. Notni, High-speed 3D shape measurement by GOBO projection of aperiodic sinusoidal fringes: A performance analysis, *Proceedings of SPIE*, Vol. 10667, 2018, 106670A.
- [20]. 3++, <https://www.3plusplus.com/>
- [21]. M. Schütz, Potree: Rendering large point clouds in web browsers. PhD Thesis, *Technische Universität Wien*, 2016.
- [22]. H. G. Maas, On the Accuracy Potential in Underwater/Multimedia Photogrammetry, *Sensors*, Vol. 15, 2015, pp. 18140-18152.
- [23]. C. Bräuer-Burchardt, C. Munkelt, M. Bleier, M. Heinze, I. Gebhart, P. Kühmstedt, G. Notni, A New Sensor System for Accurate 3D Surface Measurements and Modeling of Underwater Objects, *Applied Sciences*, Vol. 12, Issue 9, 2022, 4139.
- [24]. E. Kruck, BINGO: Ein Bündelprogramm zur Simultanausgleichung für Ingenieur Anwendungen – Möglichkeiten und praktische Ergebnisse, *International Archive for Photogrammetry and Remote Sensing*, 1984.
- [25]. T. Qin, P. Li, S. Shen, VINS-Mono: A Robust and Versatile Monocular Visual-Inertial State Estimator, *IEEE Trans. Robot.*, Vol. 34, 2018, pp. 1004-1020.
- [26]. H. Hou, N. El-Sheimy, Inertial sensors errors modeling using Allan variance, in *Proceedings of the 16<sup>th</sup> International Technical Meeting of the Satellite Division of The Institute of Navigation (ION GPS/GNSS'03)*, September 2003, Portland, USA, pp. 2860-2867.
- [27]. M. Bleier, C. Munkelt, M. Heinze, C. Bräuer-Burchardt, H. A. Lauterbach, J. van der Lucht, A. Nüchter, Visuelle Odometrie und SLAM für die Bewegungskompensation und mobile Kartierung mit einem optischen 3D-Unterwassersensor, Photogrammetrie Laserscanning Optische 3D-Messtechnik, in *Proceedings of the Beiträge der Oldenburger 3D-Tage 2022 Conference*, 2022, pp. 394-405.
- [28]. J. Sprickerhof, A. Nüchter, K. Lingemann, J. Hertzberg, A Heuristic Loop Closing Technique for Large-Scale 6D SLAM, *Automatika*, Vol. 52, Issue 3, 2011, pp. 199-222.
- [29]. J. Elseberg, D. Borrmann, A. Nüchter, Algorithmic Solutions for Computing Precise Maximum Likelihood 3D Point Clouds from Mobile Laser Scanning Platforms, *Remote Sensing*, Vol. 5, Issue 11, 2013, pp. 5871-5906.
- [30]. VDI/VDE 2634, Optical 3D-measuring systems, in VDI/VDE Guidelines, *Verein Deutscher Ingenieure*, Düsseldorf, Germany, 2008.
- [31]. C. Bräuer-Burchardt, C. Munkelt, M. Heinze, I. Gebhart, P. Kühmstedt, G. Notni, Underwater 3D Measurements with Advanced Camera Modelling, *Journal of Photogrammetry, Remote Sensing and Geoinformation Science*, Vol. 90, 2022, pp. 55-67.

## Chapter 2

# Torsion Energy to Control an Electromagnetic Plasma in a Reactor: Analysis in DC-regime and Fermionic Flow Derivations

Francisco Bulnes, J. C. García-Limón and Victor Sánchez

### 2.1. Introduction

Many papers and experimental research to design of the better geometrical shape of a reactor of electromagnetic plasma [1, 2] defined by the topological space  $\mathcal{M}_H(\sigma, \mathbf{E})$  [1], have established that the torus  $\mathbb{T}$ , of plasma can be controlled with magnetic force required to centering or guiding of the electromagnetic plasma under DC-pulse of whose spectral density of curvature (to control the plasma<sup>1</sup>) will be

$$\kappa(\omega) = \frac{q}{m_{ic}} \int_{-\infty}^{\infty} H(\xi) e^{-j\omega\xi} d\xi \quad (2.1)$$

With respect to the control function, we choice a function that keep up the magnetic field to create the current that by the Hall Effect establish a constant potential along the reactor. Remember that this is due to the existence of torsion that create the geometry of the plasma [3]. Likewise, we can choice the control with rectifier pulse  $p(\xi, \tau) = |\sin\xi|$ , and designed as:

$$u(\xi) = \begin{cases} |\sin\xi|, & 0 \leq \xi < a \\ 0, & \xi = ak, \forall k \in \mathbb{Z}^+, \end{cases} \quad (2.2)$$

---

<sup>1</sup> Remember that the curvature of an electromagnetic plasma with forces on electrical charges  $q_i$ , mass  $m$ , and constant magnetic field  $H$ , comes given by  $\kappa = \frac{q}{mc} |H|$ .

where from the electronics science perspective the control is a control of dimmer type with control of signals and electronic pulse by a semiconductor element given by the transistor 2SD882 (see the Fig. 2.1). Likewise, the control stays established by the half-wave rectifier which is obtained through corresponding Hartley's oscillator [4, 5]. Then the current is induced in the coil that induces voltage in the ferrite imam of the fly-back.

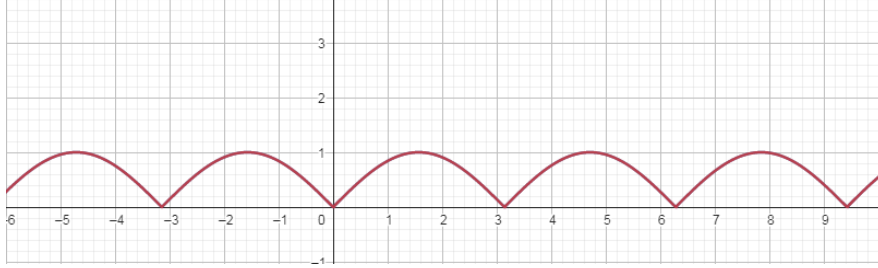


**Fig. 2.1.** Rectifier pulse used in DC.

The D882 transistor is connected to the ferrite magnet that goes to the primary coil of the fly-back in order to induce the high voltage, a characteristic of the fly-backs is that they work at high frequencies (see the Fig. 2.2 A, so it can be said that the connection of the transistor is an oscillator which produce the half-wave rectifiers [6].

Then along of torus section we can install Hall sensors to verify that the curvature energy is controlling the plasma on its cause and that the variation of the magnetic field is maintained such that at  $V_0 = 5 \text{ Volts}$  as initial condition we obtain the dynamic behavior in the Laplace transform variable  $s$ , of its integral equation:

$$U(s) = h(s) + \frac{V_0^2 H}{2\pi l^2} \int_{\xi}^{\xi} d\tau, \quad (2.3)$$

where  $U(s)$  is the function

$$U(s) = \frac{\pi a}{a^2 s^2 + \pi^2} \coth\left(\frac{as}{2}\right) \quad (2.4)$$

Then the magnetic field is controlled as (see the Figs. 2.2B, 2.3):

$$H(\xi) = |\sin \xi| + \frac{V_0^2}{2\pi l^2} H, \quad (2.5)$$

whose energy spectra is given by its curvature energy [6]:

$$\kappa(\omega) = \frac{q}{m_{ic}} \left\{ \sqrt{2\pi} \left\{ \frac{\delta(\omega-a) + \delta(\omega+a)}{2} \right\} - \sqrt{2\pi} \frac{V_0^2}{2\pi l^2} H \delta(\omega) \right\} \quad (2.6)$$

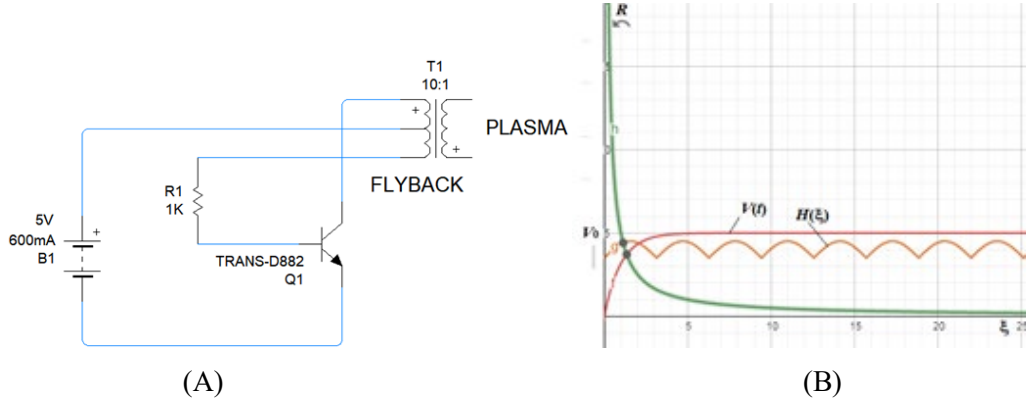


**Fig. 2.2.** (A). Circuit with data of the frequency and the output voltage. Resistive element of  $1\text{ k}\Omega$ , serves to stable the current of the plasma under feed of 5 Volts, which is regulated by the semiconductor element 2SD882. (B). The conversion DC-DC, is realized accord to the magnetic field  $H(\xi) = |\sin \xi| + 3.5$ .

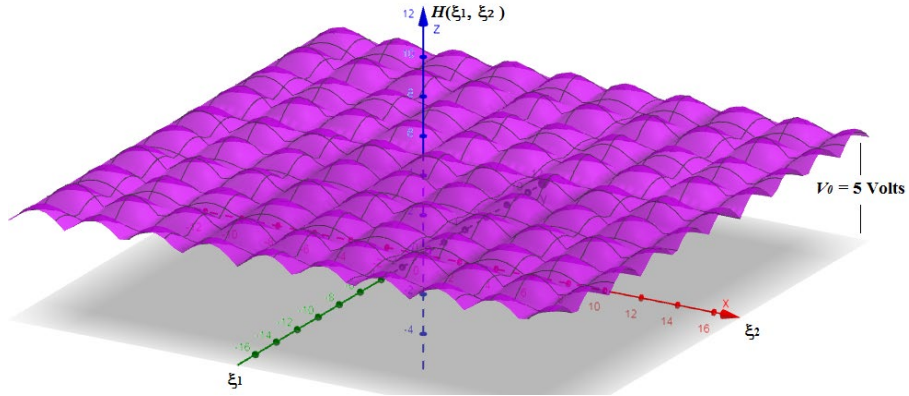


**Fig. 2.3.** 2-Dimensional surface model of the magnetic field control to electromagnetic plasma torus. The voltage feeding is  $V_0 = 5\text{ Volts}$ .

## 2.2. Electronics Experiments to Design of a Device Control

We realize several experiments to show the importance of the magnetic field, being this, an angular piece of the curvature control to keep the plasma captive and aligned circulating in the toroidal enclosure; which, as has been demonstrated, is the space with the proper and necessary topology for the configuration and design of the reactor [1, 7].

Also, as we said, the direct current regime is the best to create a best response and curvature control as given in (2.6) with the energy properties more adequate to the signal of permanent energy necessary to continuity and consistency of the plasma. Then experiments under direct current regime are necessary to evidence the torsion energy (see Figs. 2.4A, 2.4B) like fundamental part in the behavior of the electromagnetic plasma and

its control through curvature energy with magnetic intensity field. Remember that the evidence is with appearing of the signals  $\frac{\sin a\omega}{a\omega}$ , or  $\frac{\cos a\omega}{a\omega}$ ,  $\forall a \in \mathbb{Z}$ , [8].

For other way, and using the control developed in the section 1, under direct current regime, we have the control unit consistent of a current dimmer with control of signals and electronic pulse  $p(\xi, t)$ , by a semiconductor element given by the transistor 2SD882.

After to derived fermionic products from the electromagnetic plasma we consider a *zvs-circuit* to control the fermionic flow obtained and produce the shock-wave to generate the impeller force. The zvs-circuit used is the following Figs. 2.5, 2.6A, 2.6B.

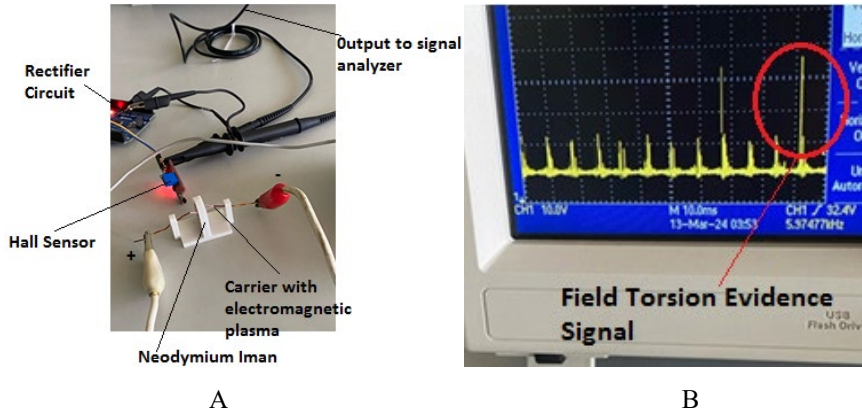


**Fig. 2.4.** (A). Electronic experiment considering a Hall sensor to detect field torsion evidence signals, when is carried electromagnetic plasma through filament of conductor (carrier) under magnetic field of Neodymium magnet, and sensing through Hall sensor, (B). Outputs of field torsion evidence signals in the screen.

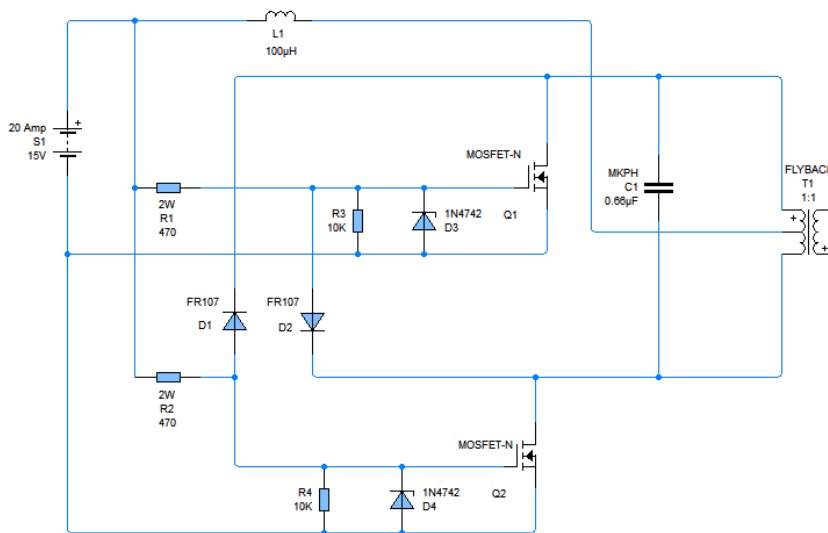
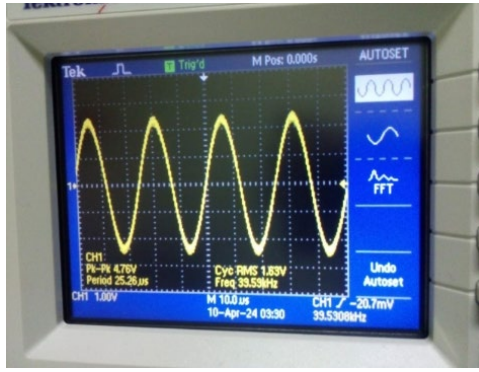


**Fig. 2.5.** The zvs-circuit.



A



ZVS

B

**Fig. 2.6.** (A). Screen of the oscilloscope showing the constant high frequency to control of the direct current regime, (B). zvs-circuit unit with inductor element to control the fermionic flow derived from the high current of 20 A.

### 2.3. Derived Fermionic Products

We consider the derived fermion products from the electromagnetic plasma, which form three classes of electron derived products (see the Fig. 2.7) where the last step are ions, which could be used in ionic propulsion.

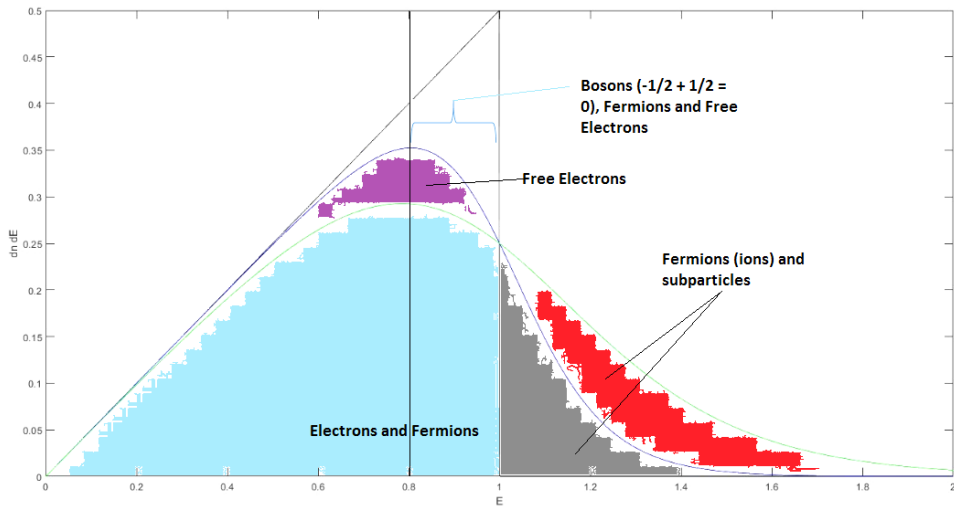


**Fig. 2.7.** Occupation-number of total Electrons-fermion in three phase distribution  $n(r, t)$ . The third phase corresponds to the ions that will be pure fermions: as sub-particles as leptons, anions, and etcetera.

Then have considered the plasma physics in three fundamental aspects of study; its magnetic managing and control, where are analyzed the congruences modulo



conductivity, that are the topological spaces  $\sim II_H(\sigma, \mathbf{E})$ , [9, 10], and the current quality, which give us the velocity of charge carriers and the fermion derived products that can be used in ionic propulsion as another alternative to a flying ship, when is considered the plasma as ionized gas or fluid, where the MHD framework can be used. In the frame to stabilize the current is used a fly-back and from a point of view of electronics, is created a control of current from a current dimmer with control of signals and electronic pulses  $p(\xi, t)$ , by a semiconductor element given by the transistor 2SD882. The dynamical system was analysed obtaining that the control through magnetic field is given by the curvature with a curvature energy  $\kappa(\omega)$ , given by (2.6), which arises considering the embedding in an ionized space determined by the mapping  $\sigma: M \rightarrow \sim II_H(\sigma, \mathbf{E})/M$ , which is possible due to the topology of the plasma [6].

If we want the impulse force, we must consider the rarefaction equal to zero, thus the pressures  $P_{i,e} = 0$ ,<sup>1</sup> and  $gradP = 0$ . Further the total fermionic action is a sum of the actions of the ions that are fermions and electrons which derive fermions too.

A propeller from the electromagnetic plasma now fed through DC-current, is created and designed showing very advantages on AC-current feeding reactor [2, 6].

**Lemma 2.1.** In all MHD process

$$\sim II_H(\sigma, \mathbf{E}) = \sim II_e(\sigma^2, \mathbf{j}) \quad (2.7)$$

*Proof.* [6]. ■

In the demonstration was considered as strong argument the identity between topological spaces considering a considerable direct current  $\mathbf{j}$

$$\sim II_H(\sigma, \mathbf{E}) = \sim II_e\left(\sigma, \frac{\mathbf{F}}{e}\right) = \sim II_e(\sigma^2, \mathbf{j}) \quad (2.8)$$

Only with the square of the electric conductivity can be possible to obtain sufficient current with charge carriers.

Likewise, we consider  $M \subset \sim II_e(\rho, \mathbf{v})$ , a space where we will design our camera of ions concentration (see the Fig. 2. 8) to realize the propulsion:

$$M = \{\rho | \rho = n_i m_i + n_e m_e\} \quad (2.9)$$

This camera consists of the section of negative connection in an ionic propeller whose reactor is an electromagnetic plasma  $\sim II_H$ , which is transformed in an ionic gas (ionic wind) which has an impulse force (see the Fig. 2.9).

---

<sup>1</sup>  $P_{i,e}$ , and  $P_{e,i}$ , are interacting forces due to the collisions of the electrons on ions and ions on electrons respectively.

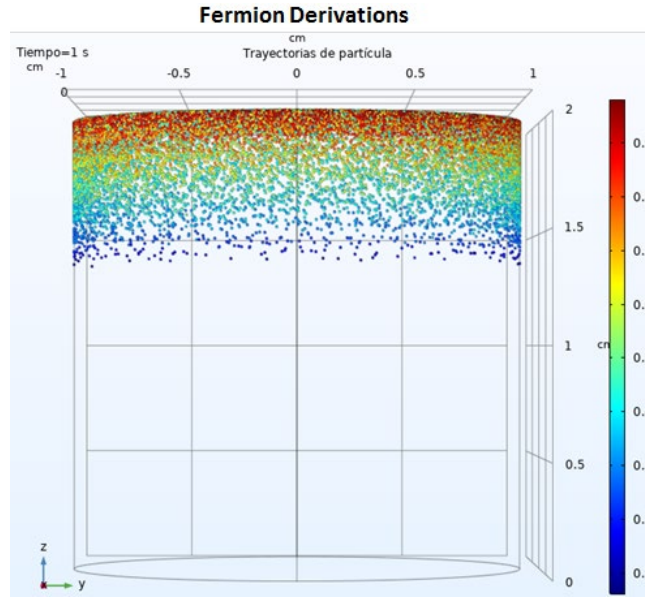


**Fig. 2.8.** Electron density from the electromagnetic plasma and its derivations in fermions, until to obtain fermions with high velocity (ions) and few free electrons. The red color is a mixture of electrons and photons, yellow stills being mixture where the prevalence is marked by photons. After the photons that are fermions interacts nulling creating bosons. Finally remain ions are fermions with high velocity and few free electrons.

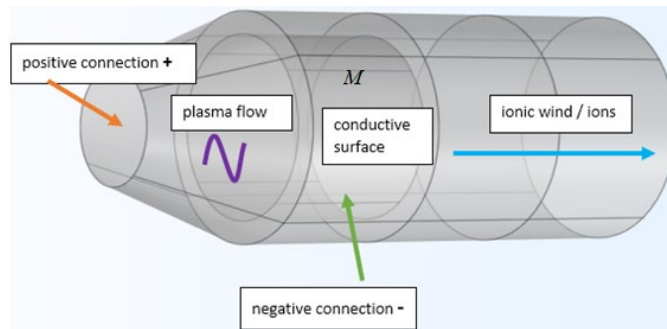


**Fig. 2.9.** The negative connection section is the ions concentration camera.

Then we can simulate the impeller fermion products and their behavior under an ionic propeller designed as has been showed in the Fig. 2.9, where we can identifier two three phases concordant with the fermion classes distribution mentioned in the Fig. 2.7. These phases are: the plasma flow derived step, the conductive surface (surface charged negative) and the ionic wind (ions) that is the ionic propeller flow. This obeys to the topological disposition obtained when  $\mathcal{H}_e(\rho, v)$ , is the ternary mixture or ionized gas space conformed of electrons, ions and fermions. This can be formulated as the topological vector homogeneous space (Figs. 2.10A, and 2.10B):

$$\sim II_e(\rho, \mathbf{v})/M = \left\{ \mathbf{v} \mid \mathbf{v} = \frac{1}{\rho_m} (n_i m_i \mathbf{v}_i + n_e m_e \mathbf{v}_e) \right\} \quad (2.7)$$

Then we can state:

**Proposition 2.1.** If we consider  $n_i = n_e$ , then the total force of the ionic flow in  $\sim II_e/M$ , is:

$$F_i = -n_i m_i \mathbf{g} + q \left( \mathbf{E} + \left( \frac{1}{c} \right) \mathbf{v}_i \times \mathbf{H} \right) \quad (2.8)$$

Proof. [6].■

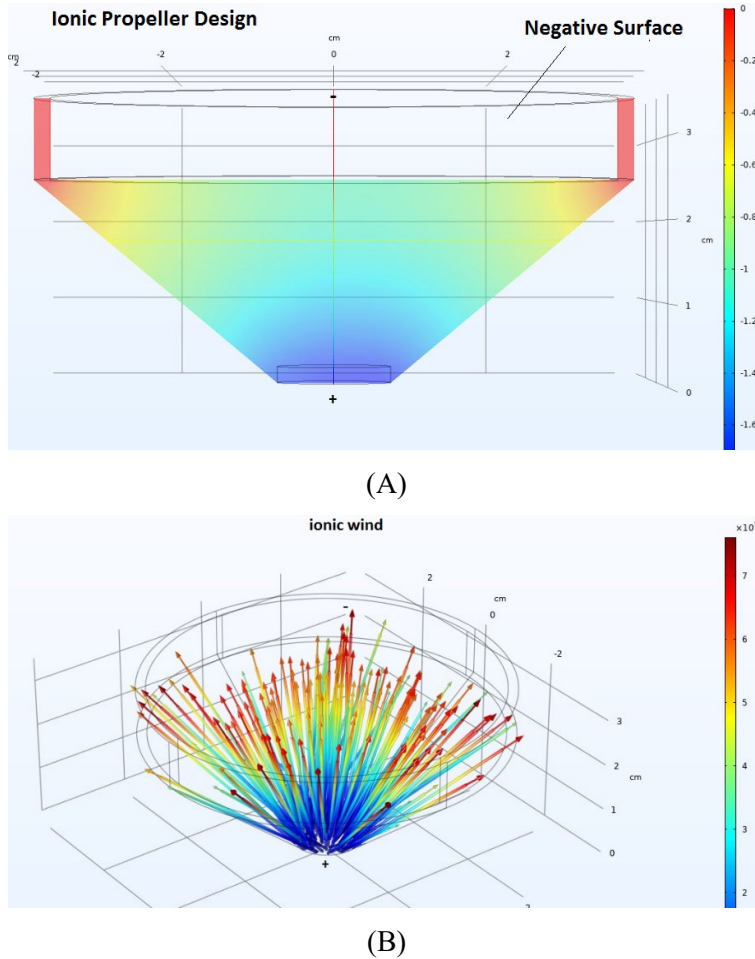


**Fig. 2.10.** A). Design of ionic propeller section, B). “Ionic wind” obtained under concentration of fermion derived products (+ → -).

This force must be guided and compressive to increase it (possibly through shock devices and magnets) as propulsion force enough to displace a vehicle and have it flying.

Also was made another proof where we intent “compress” or realize “magnetic pressure”<sup>1</sup> on the ions through magnetic fields (obeying the control theorem by curvature energy given by its magnetic intensity to a plasma in this case a gas plasma of particles). Likewise, this magnetic field action on ions consists basically in imans located between electrodes where is produced the ionic effect (Fig. 2.11A, 2.11B).

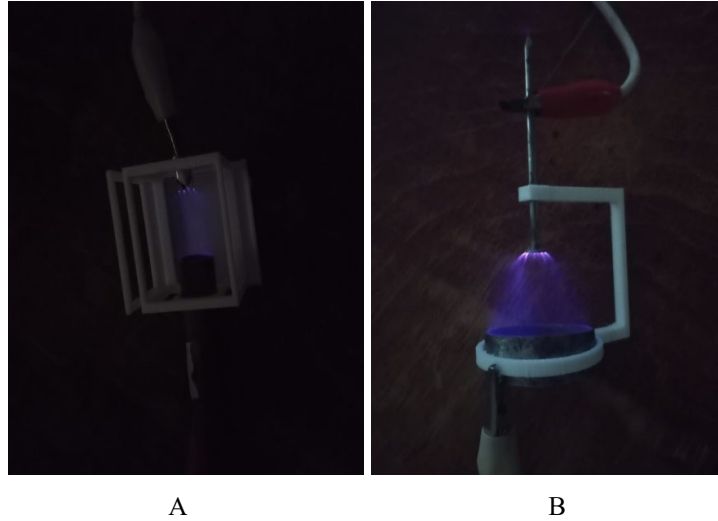


**Fig. 2.11.** (A). Magnetic box showing the fermion derivation flow (“ionic wind”) from a little tubular section which is aligned due the magnetic walls in this special camera. (B). Outside the magnetic camera, and reproduction the same electrical conditions considering a point a tubular section to see the behavior of the “ionic wind”.

The imans used are of 0.1 Teslas, which are 1000 Gauss, no much field, however in this case are eight Neodymium imans located around of the ions (see the Fig. 2.12).



**Fig. 2.12.** Propeller with Neodymium imans.

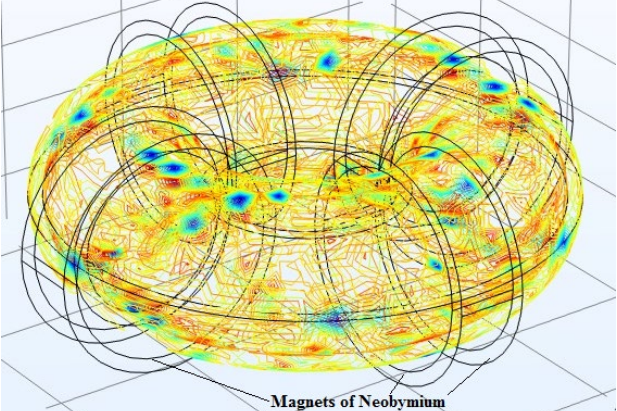
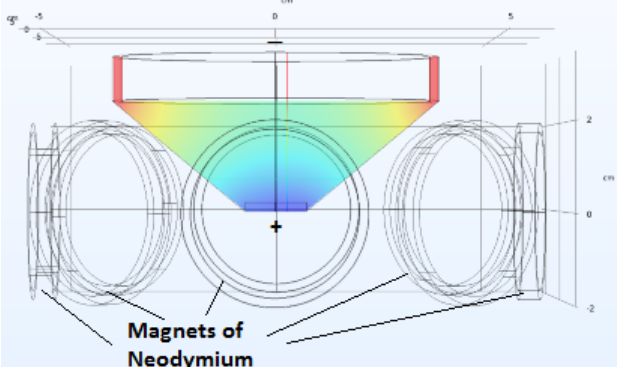
---

<sup>1</sup> This term “compression” is valid due that the thermodynamics framework is the Boltzmann equation. The plasma here is derived as plasma gas.

Likewise as stability, control, high velocity of its charge carriers and power to the construction of a reactor, are some of these advantages, where could be included much other applications in addition a flying ship.

The magnetic disposition in the reactor and propeller plasmas can be illustrated in the following Table 2.1.

**Table 2.1.** Magnetic Disposition of magnets to control of two electromagnetic plasma types.

Plasma	Magnetic Disposition and Plasma Flow
Electromagnetic Plasma	
Ionic Gas Plasma	

## 2.4. Conclusions

The electromagnetic plasma study has conducted to another logical alternative deduced from the proper field theory of the plasma, and its derived products as free electrons and fermions, which considering certain conjectures and formal statements establish the possibility of the ionic propulsion, considering the transformation of the electromagnetic plasma like an electronic gas plasma rich of fermions determining three fundamental mixtures until the step of propulsion. The Lemma 2.1, and Proposition 2.1, establish the total Newtonian force that must expeller in the ionic propeller that is to say the topological vector space of the velocities required of the ions in propeller. The control to the two

plasma types always will be a magnetic field with sufficient intensity to establish a curvature energy control of the plasma in each case. The feeding of the whole energy comes from the reactor which will be the principal energy feeding of the vehicle or ship. The following step will be given a prototype that can moves and displaces.

## Technical Notation

$\sim II_H(\sigma, \mathbf{E})$ : Topological space of the electromagnetic plasma characterized by the conductivity  $\sigma$ , and electromagnetic field E-H.

$\sim II_e(\rho, \nu)$ : Topological space of the electromagnetic plasma in the ternary mixture or ionized gas space conformed of electrons, ions and fermions.

$\kappa(\omega)$ : Curvature energy or curvature spectra used to characterize the control energy in the control of electromagnetic plasma.

$\sim II_e(\rho, \nu)/M$ : Topological vector homogeneous space used to characterize the propeller and electromagnetic plasma as ionized gas.

$M$ : Camera of ions concentration to realize the propulsion. Defines the propeller and ionic gas.

$p(\xi, t)$ : Electronic pulse given by a semiconductor element that define a control and rectifier transistor.

DC: Direct current regime.

$F_i$ : Total force of ionic flow in the propeller (plasma modulus camera of ions concentration).

$M$ : Camera of ions concentration to realize the propulsion.

## References

- [1]. F. Bulnes, J. C. García-Limón, V. Sánchez, L. A. Ortiz-Dumas, Electromagnetic plasma reactor: Implicit application of field torsion I, *Int. J. Electron. Microcircuits*, Vol. 1, Issue 1, 2021, pp. 30-35.
- [2]. Dr. F. Bulnes, J. C. García-Limón, V. Sánchez, L. Alfredo Ortiz, M. Flores, A. García, Electromagnetic plasma reactor: Implicit application of field torsion II, *Int. J. Electron. Microcircuits*, 2022, Vol. 2, Issue 1, pp. 01-09.
- [3]. N. C. Little, Magnetohydrodynamics, *Van Nostrand Inc*, New York 1967.
- [4]. M. A. Salam, Q. M. Rahman, Fundamentals of Electrical Circuit Analysis, *Springer*, 2018.
- [5]. U. Tietze, C. Schenk, E. Gamm, Electronics Circuits: Handbook for Design and Applications, *Springer*, 2015.

- [6]. Dr. F. Bulnes, J. C. García-Limón, V. Sánchez, L. A. Ortiz-Dumas, Electromagnetic plasma reactor: Implicit application of field torsion III: Derived ionic flow, *Int. J. Res. Adv. Electron. Eng.*, Vol. 3, Issue 2, 2022, pp. 87-92.
- [7]. Dr. F. Bulnes, J. C. García-Limón, V. A. Sánchez-Suárez, L. A. Ortiz-Dumas, M. Y. Flores-García, A. U. García Galicia, Fine measurements of field torsion and its spectra, in *Advances in Sensors Reviews*, Vol. 8, Sensors, Measurements and Networks (S. Yurish, Ed.), *IFSA Publishing*, 2022.
- [8]. Dr. F. Bulnes, J. C. García-Limón, L. A. Ortiz-Dumas, V. A. Sánchez-Suarez, Detector of torsion as field observable and applications, *American Journal of Electrical and Electronic Engineering*, Vol. 8, Issue 4, 2020, pp. 108-115.
- [9]. M. Alonso, E. J. Fin, *Fundamental University Physics*, Vol. 3, Quantum and Statistical Physics, *Addison-Wesley Publishing Company*, 1968.
- [10]. G. Wolschin, Local equilibration of fermions and bosons, *Results in Physics*, Vol. 13, June 2019, 102197.

## **Chapter 3**

# **A Low-cost and Flexible Prototype for Static and Dynamic Calibration of Pressure Measurement Channels**

**José Dias Pereira, Artur M. F. Graxinha, Octavian Postolache and Vítor Viegas**

### **3.1. Introduction**

Time-varying pressure measurements with high accuracy are essential for numerous applications. Pressure sensors frequently need to be placed at specific distance away from the measuring taps due to temperature values, very high or very low, easy access for maintenance, reliability, robustness against harsh working conditions, among others reasons [1]. The pressure transmission line, such as a capillary, an impulse line or a pneumatic tube, to connect the pressure sensor to the measurement point is, consequently, an important part of the pressure measurement channel. Thus, the accuracy of dynamic pressure measurements can be greatly impacted by the dynamic characteristics of the pressure transmission line, by the internal volume of the pressure transducer, by the material and geometric properties of the connecting transmission line and by the thermodynamic and transport properties of the transmission medium [2]. For these reasons, the frequency response of the transducer must be considered together with the frequency response of the other elements included in the pressure measurement channel. Considering, as an example, that exist only capillary effects, according to National Institute of Standards and Technology [3-5], when high frequency dynamic pressures are to be measured, there are many factors that should be properly taken into consideration. When the pressure signal reaches the sensing device, there are two main types of distortions, namely, the transmitted pressure signal could be affected by phase distortion, altering any time correlations that can exist in the original signal, or the amplitude of the pressure signal could be distorted, selectively in frequency, causing large measurement errors. An example, of the last kind of errors occur if a resonance condition exists within



the pressure transmission line and the pressure signal variations activate those resonances [6]. So, the importance of dynamic calibration is not restricted to specific applications, such as military engineering, chemical explosion tests [7], petroleum exploration and well testing [8], gas turbine testing and combustion engine testing [9-10], among others, but are also important in industrial and biomedical applications. One industrial application where dynamic calibration of pressure sensors is crucial is related with the measurement of pressure pulsations in the headbox feed pump of a paper machine [11]. Pressure pulsations, generated at the headbox feed pump, might create unacceptable variations of paper basis weight in the machine direction affecting strongly paper quality and process efficiency. Thus, in pressurized headboxes, pressure measurements must be very accurate and the dynamic characteristics of the pressure measuring channel are critical. Other typical example of dynamic calibration in industrial applications, is related with the need to assure a pump net positive suction head in order to avoid pump performance drop caused by cavitation [12]. It is very important to maintain pump suction pressure as constant as possible. One way to achieve this purpose is to connect the pump suction input to a tank where a constant level control is implemented, using differential or relative pressure measurement transmitter. A last, but also important example of the importance of dynamic pressure measurements in industrial applications, is related with boilers efficiency. Thus, an accurate control of the amount of air is essential to boiler efficiency since too much air will cool the furnace, and carry away useful heat, and with too little air the combustion will be incomplete, unburned fuel will be carried over and smoke may be produced. To avoid these problems, air flow measurement, commonly implemented by differential pressure sensors, is essential to control the blower operating point. Thus, the air flow measurement that is affected by a large number of dynamic disturbances, such as, direction and intensity variations of the wind, must be dynamically accounted to improve boilers' performance. To conclude the importance of dynamic pressure measurements, it is important to also refer biomedical measurement systems. For example, in blood pressure measurements, the dynamic pressure signal contains much more information than the two common steady state values of systolic and diastolic pressures [13] being required to access its dynamic contents. Additionally, in ergonomics area there is an interest to measure the pressure distribution, as well as, the total force between hand and tool during some operations [14]. Furthermore, in physiotherapy, the measurement of foot pressure during the walk is also very important to perform gait analysis requiring the usage of dynamic and accurate pressure sensors [15].

### **3.2. Calibration**

In general, the performance, accuracy and performance of pressure sensors, in a variety of applications, depend on both static and dynamic calibrations. Static calibration guarantees accuracy in steady-state conditions, while dynamic calibration evaluates the sensor's capacity to react to abrupt pressure changes, being essential for real-world applications where pressure variations happen often.

### 3.2.1. Static Calibration

The pressure is said to be static when it remains constant for a significant amount of time, generally during several multiples of a complete measurement period. Fig. 3.1 depicts the working principle of a typical deadweight tester for static calibration purposes. The majority of dead weight testers are found in calibration facilities or laboratories across almost all industrial plants. A dead weight tester compares the pressure that a known weight exerts on known surface using directly pressure definition and Pascal's principle. Thus, a dead weight tester has a reservoir chamber filled with oil, that is almost incompressible, a primary piston that carries a known weight, an isolation valve for the oil reservoir, known weights of varying magnitudes, and a secondary piston that applies pressure to the oil in the chamber. The device under calibration is a pressure transmitter, gauge, or a pressostat. It is important to refer that this static calibration method enables an expanded relative uncertainty [16] of some tens of p.p.m., under controlled environmental conditions.

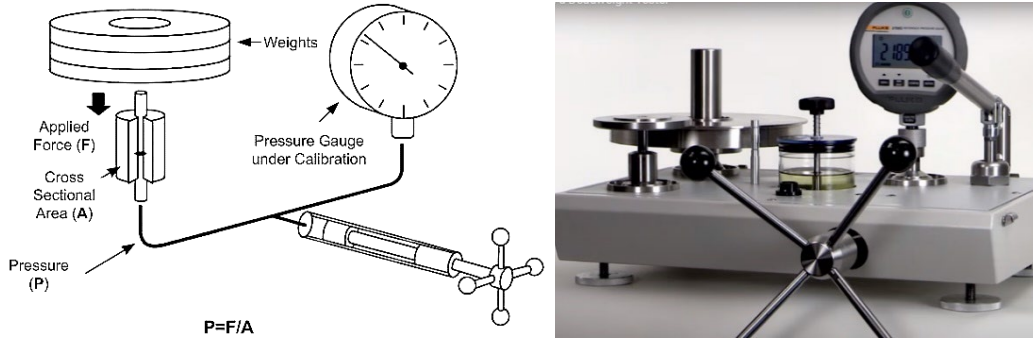


Fig. 3.1. Working principle of a typical dead weight tester frequently used for static calibration.

### 3.2.2. Dynamic Calibration

Even if, till nowadays, there are still no traceable dynamic pressure calibration standards, except for sound pressure, dynamic calibration of pressure sensors can be obtained, in time or frequency domains, using different methods. It is very important to establish the border between the cases where static calibration is an acceptable solution, from the cases where dynamic calibration is essential to avoid large measurement errors. Obviously, the line border between the need of static or dynamic calibration, depends on the frequency behavior of the measurement channel, on the maximum frequency of the measurement signal and on the maximum calibration error that can be accepted for a given application. Since, the measurement channel is typically modelled as a second order system, which is a common approximation for the pressure measurement channel it makes sense to define the border line according to maximum measurement error that is acceptable in a given application. Thus, considering the transfer function of a second order system defined by:

$$G(s) = \frac{G_0 \cdot \omega_n^2}{s^2 + 2 \cdot \zeta \cdot \omega_n \cdot s + \omega_n^2}, \quad (3.1)$$

where  $G_0$  represents the static gain,  $\zeta$  the damping factor and  $\omega_n$  the natural frequency. From (3.1), it can be deduced the relationship between the maximum acceptable error and the damping and natural frequency of the second order system. Fig. 3.2 represents the measurement error amplitudes that are obtained in a dynamic pressure measurement system if only static calibration performed.

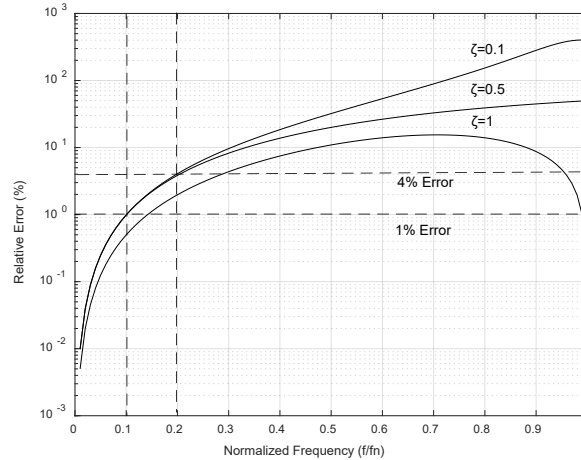


**Fig. 3.2.** Relative errors associated with the usage of static calibration when the measurement channel has a second order low-pass filter characteristic ( $f$  is a signal frequency;  $f_n$  is a measurement channel natural frequency;  $\zeta$  is the damping coefficient).

As it is clearly visible in previous figure, the relative errors that are obtained can be very large if the signals to be measured are affected by channel's behavior in terms of its transfer function characteristics, namely, damping and natural frequency. The relative error as a function of the normalized frequency, for low values of the damping coefficient, is about 1/10 and 1/5 of the pressure channel natural, for an acceptable threshold error equal to 1 % and 4 %, respectively.

Regarding dynamic calibration methods, the pressure generator may produce either a periodic or an aperiodic pressure. According application requirements, harmonic periodic pressure generators are used in pressure measurements with periodic or repetitive characteristics and, on the other hand, for example, it would make sense to use an aperiodic pressure generator, such as shock tubes, fast opening devices, or falling weights [17] if the measurement system is used to measure impulsive pressure pulses. When a transducer experiences negative step loading stimulus, that means if it is subjected to an abrupt pressure shift from a known static pressure value to either ambient pressure or vacuum, it is recommended to use fast-opening devices, such as a valve that vents the pressure chamber to air pressure or vacuum, respectively. Nowadays, a pressure release time of a few milliseconds can be achieved using this type of devices.

### 3.3 Pressure Measurement Channel

Pressure transmitting lines, usually based on capillaries, pneumatic or impulse lines, are used to enable the location of pressure transmitters away from the process being measured so as to reduce the negative impact of the temperature on the transmitter's performance and operating life. Locating the pressure transmitter away from the process can also reduce the adverse effects of vibration and facilitate access to the transmitter for replacement or, in some cases, enable its adequate maintenance. However, there are also several negative impacts caused by the usage of pressure transmitting lines. Since the measurement points, typically known as pressure taps, are away from the sensor and signal conditioning circuits, being additional sources of errors introduced in the measurement channel. These measurement errors are particularly serious if dynamic pressure measurements are being performed but they also occur, obviously, in static pressure measurements. The response time of a pressure transmitting line is mainly affected by two types of delays: the sonic delay, correspondent to the time that it takes for the pressure signal to travel at the speed of sound through a pneumatic line or through a completely filled line; and the hydraulic delay that depends mainly on the volume of fluid that must be moved in the pressure transmitting line to bring a pressure change in the sensing element of the transmitter. Thus, it is important to underline that the dynamics of a pressure measurement channel does not depends only on the dynamics of the measuring transducer but also on the dynamic of the pressure transmitting line and also on the dynamic characteristics of the signal conditioning circuits. Usually, the natural frequency given in the transducer specifications is only the mechanical natural frequency of the pressure sensing diaphragm without considering the crucial dynamic limitations associated with the capillaries and transducer sensing cavity volume. Considering, as an example, a typical pressure measurement channel, represented in Fig. 3.3, the transducer may be dynamically calibrated and even if it is known that all transducer natural frequencies are far above the frequency content of the pressure to be measured, the inclusion of a capillary or pneumatic tube, between the pressure taps and the pressure input ports of the measuring transducer, changes the situation completely by introducing a significant low-frequency dynamic element. In these cases, the pressure signal applied to the pressure transducer does not resembles the pressure signal under measurement, particularly when dynamic pressure signals are at stage. This problem can't be ignored since the main dynamic limitation are typically associated with the frequency limitations of the capillary or pneumatic tube that interconnects the pressure measuring tap to the sensing transducer cavity volume.

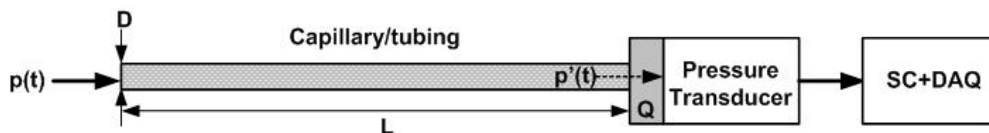


**Fig. 3.3.** Pressure measurement channel ( $p(t)$  is the input pressure signal;  $p'(t)$  is the pressure signal at the input of the pressure transducer;  $L$  is the capillary/pneumatic tube length;  $D$  is the capillary/pneumatic tube diameter;  $Q$  is the transducer cavity volume; SC is the signal conditioning; DAQ is the data acquisition).

The dynamics of the tubing can be modelled by the Helmholtz resonator model or by the organ pipe model [18], but to obtain accurate information about the dynamic characteristics the measurement channel must be calibrated. The flat frequency bandwidth of the pressure measurement channel depends mainly on the geometry and construction of the pressure sensor, on pressure transmission line dimensions, on the fluid media inside the transmission line and on the output filtering of the conditioning circuits. As a rule of thumb, regarding the frequency bandwidth limitations at the transducer level, it is important to refer that the maximum frequency of the dynamic pressure signal at transducer's input should not exceed one-fifth of the natural frequency of the reference transducer in order to assure measurement errors lower than four percent. Regarding the conditioning circuit response, it is important to underline that damping parameter that is generally used to parametrize the transmitter has a direct impact on the dynamic response of the pressure measurement channel. High damping values filter out process noise at expenses on the useful pressure channel bandwidth. Thus, regarding dynamic calibration, it is important that transmitters' damping is deactivated or, if not possible, that the shortest possible time constant setting is selected. The natural frequency of the capillary plus the sensor cavity of the pressure transducer can be given, approximately by [19-20]:

$$\omega_n = \frac{c}{L \cdot \sqrt{\frac{1}{2} + \frac{4Q}{\pi \cdot D^2 \cdot L}}}, \quad (3.2)$$

where  $c$  represents the sound velocity in the medium contained inside the capillary;  $D$  represents the internal capillary diameter;  $Q$  represents the sensor cavity volume and  $L$  represents the capillary length. By its turn, the damping coefficient of the pressure measurement channel can be approximated by [19]:

$$\tau = \frac{16 \cdot \mu}{D^2 \cdot \rho \cdot \omega_n}, \quad (3.3)$$

where  $\mu$  represents the capillary fluid dynamic viscosity;  $D$  represents the internal capillary diameter;  $\rho$  represents the capillary fluid density and  $\omega_n$  represents the natural frequency of the capillary plus the sensor cavity volume. From (3.2) and (3.3), it is possible to conclude that there is a compromise in the product of the damping coefficient times natural the frequency of the pressure measurement channel that does not depend on the capillary length and that varies inversely with the square value of the capillary diameter.

### 3.4. Calibration Prototype

In the next paragraphs the hardware and software parts of the calibration prototype will be presented. The proposed low-cost prototype can be used as a periodic or aperiodic pressure generator being possible to perform time and frequency characterization of a dynamic pressure measurement channel in the low-medium pressure range. The developed prototype is mainly based on an electro-pneumatic pressure regulator (EPPR) and works, basically, as an arbitrary waveform pressure generator for pressure amplitudes lower than 10 p.s.i. This pressure range can be extended using EPPR devices with a larger

pressure output range. It is also important to underline an innovative capability of the proposed calibrator that consists on its ability to regulate its output according to the real pressure values that are applied to the remote pressure transducer that is under calibration. This advantage is particularly important to avoid errors caused by any fluid leakage that can exist in the pressure measurement channel, namely, in the pressure transmission line that interconnects the pressure measuring tap to the remote transducer. Apart from the previously mentioned benefits, of the proposed prototype, it must be underlined that the accuracy that can be achieved is not as high as the accuracy and measuring range that can be achieved with some commercial dynamic calibrators [21-23] that use, either, time or frequency calibration methods being not possible to use both methods in the same calibrator.

### **3.4.1. Hardware**

Fig. 3.4 represents the basic block diagram of the electropneumatic pressure regulator (EPPR), used to generate pressure signals for static and dynamic calibration. The main components of the block diagram include: a pneumatic pressure transducer (PT1), a miniature electrovalve with vent capability, used to speed up the pneumatic discharge of air and for zero calibration purposes, a miniature proportional valve (MPV) and some elementary signal conditioning circuits, namely, a comparator and a voltage follower. The setpoint signal, used to define the pressure to be applied to the pressure device under test (PDUT), is generated by a multifunction data acquisition board with 12-bit resolution; a maximum sampling rate of 50 kS/s and a variable DAC output voltage range between 0 and 5 V. The two inputs and three outputs of the EPPR block are, respectively: the control voltage (“setpoint”) of the pressure EPPR output, whose value varies between 0 and 5 V; the air supply (AS); the output pressure monitoring signal (MPS), also variable between 0 and 5 V; the air exhaust outlet (VENT) and the interconnection terminal to the PDUT under test or calibration. Connecting the EPPR device to a PC equipped with a multifunction data acquisition board (PC+DAQ), it is possible to generate calibration signals with different amplitudes, frequencies and waveforms, including arbitrary waveforms. In this way, for each pressure value, required for static or dynamic calibration purposes, the calibration routine sequence include the following steps: the program installed in the PC calculates the corresponding voltage value, for a given pressure value, and the multifunction board output the calibration voltage to the EPPR setpoint voltage input; the EPPR imposes an output pressure value that is a function of the setpoint voltage of the electronic control circuit; the monitoring pressure signal (MPSS) is compared with the pressure signal applied to the PDUT and the difference between these pressure values is compensated by a feedback control loop. Regarding the main characteristics of the pressure sensor [24] used for feedback sensing purposes it includes a measuring range between 0 and 5 p.s.i. and a response time of 1 ms.

An important advantage of the proposed calibration prototype is that it can be used to test field located equipment without need to disconnect the capillaries, or impulse lines, which means that the working conditions of complete pressure channel are not changed during calibration. Additionally, the remote pressure sensing capability of the proposed prototype enables the compensation of the errors associated with pressure drops, such as the typical

errors caused by leakages in the pressure transmission line and associated mechanical tubing connectors and interfaces. As limitations of the proposed calibration system, it must be referred that the time response of its components limits the maximum value of the working frequencies to a few hundreds of Hertz and the pressure amplitudes to a few hundreds of kPa.

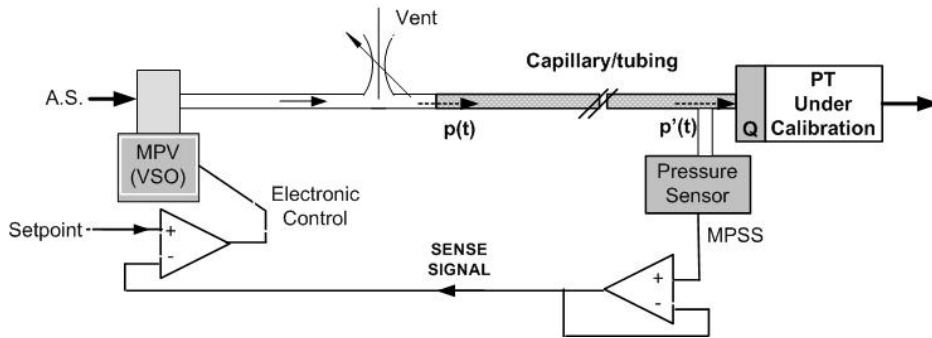


**Fig. 3.4.** System hardware block diagram (A.S. is an air supply; MPSS is the monitoring pressure sensor signal; PT is a pressure transmitter; MPV is a miniature proportional valve).

### 3.4.2. Software

Several procedures for configuring the calibration signal, processing data for evaluating static and dynamic calibration parameters, storing calibration data, and producing calibration reports are all included in the software of the proposed pressure calibrator. Almost all software routines were developed using the LabVIEW graphical program language. Fig. 3.5 represents the front panel of the virtual instrument (VI) that is used to parametrize the pressure signal, used for calibration and testing purposes. The main configuration parameters, displayed in the VI front panel include the pressure signal waveform, its frequency and amplitude, and the offset of the control voltage signal that is applied to the setpoint input of the EPPR device. The main attributes of the pressure calibration signal include the number of bursts, the number of pulses within each burst, the duration of the inter-burst pause, and a burst modulation parameter. In the example represented in Fig. 3.5, the pressure calibration signal consists of two burst patterns, seven pressure pulses per burst, a second inter-burst pause, a triangle pattern waveform with frequency equal to 5 Hz, amplitude equal to 1 V and an offset equal to 2.5 V.

Additional routines of the developed software are used to perform static calibration, diagnostic tests of the hardware, namely of the EPPR device, to collect calibration results from the PDUT and to store measurement and historical calibration data obtained, over the time, for the same PDUT. This data is particularly important in industrial applications to defined the cycle of the routine maintenance tasks and to implement condition-based maintenance. Fig. 3.6 represents the block diagram that implements the main routine of the LabVIEW virtual instrument (VI) previously referred.

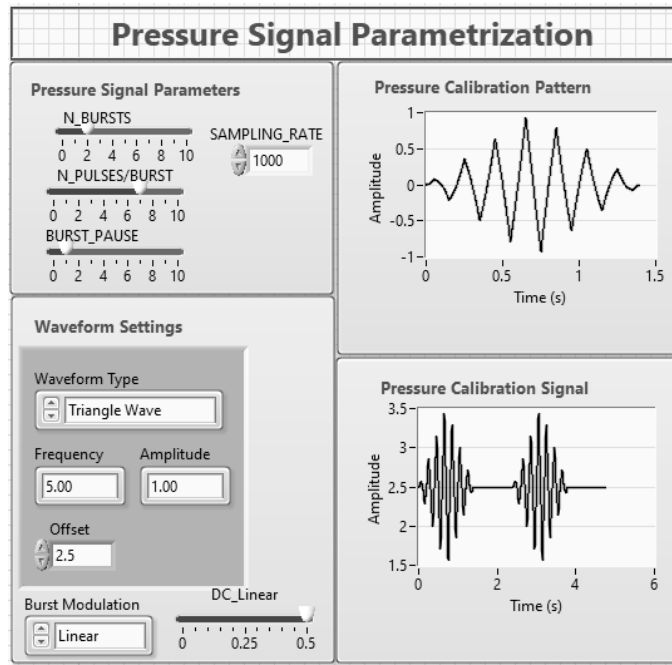


Fig. 3.5. Front panel of the LabVIEW virtual instrument used to parametrize the calibration pressure signal.

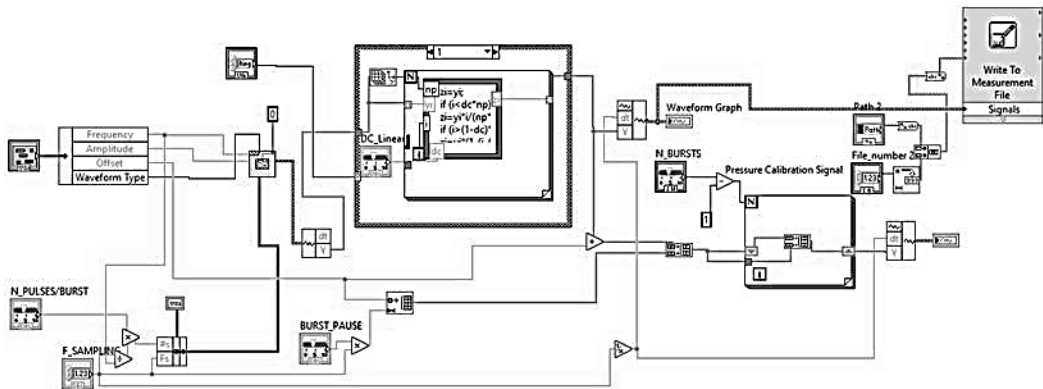


Fig. 3.6. Block diagram of the LabVIEW virtual instrument used to parametrize the calibration pressure signal.

### 3.5. Experimental Results

The present section includes two application cases to demonstrate the capabilities of the presented prototype. One case is related with the testing and calibration of a pressure transmitter, connected through a pressure transmission line to our prototype, and the other case is related with the calibration of an automatic oscillometric sphygmomanometer.



### 3.5.1. Industrial Pressure Transmitter

In order to experimentally verify the importance of the frequency characterization of the pressure measurement channel, when pressure dynamic measurements are performed, the proposed calibration prototype was used to generate pressure variations with different waveforms, amplitudes and frequency contents. Both calibration methodologies, in time and frequency domains, were considered. Fig. 3.7 represents the test set up used to perform a dynamic calibration of a pressure transmitter that is remotely connected to the calibrator through a pneumatic tube.

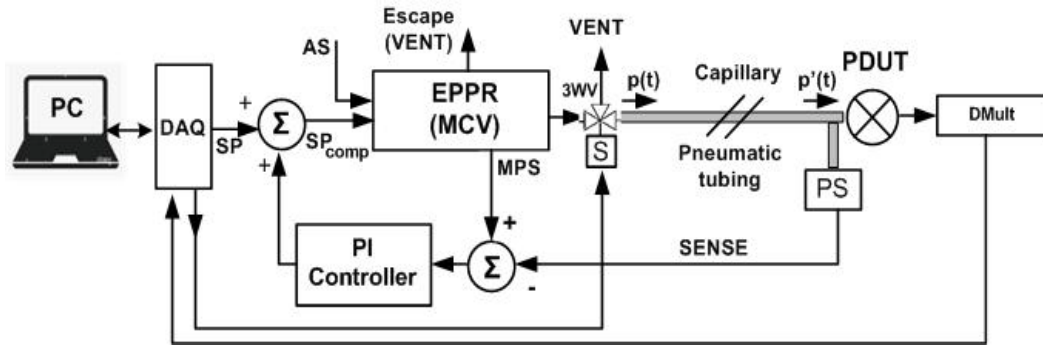


**Fig. 3.7.** Testing block diagram used to evaluate the dynamic behavior of a pressure transmitter (PDUT is a pressure device under test; SP is a setpoint; DAQ is a data acquisition board; DMult is a digital multimeter; PS is a pressure sensor used for pressure sensing purposes; 3WV is a 3-way electric solenoid valve; EPPR is an electropneumatic pressure regulator; MCV is a miniature control valve; PIC is a proportional and integral controller; S is a 3-way electrical valve control signal).

The main elements of the testing block diagram include: the pressure transmitter to be calibrated [25]; the prototype calibrator previously described; a 3-way electric solenoidal valve [26]; the capillary or pneumatic tubing; the pressure sensor used for remote sensing of PDUT applied pressure; a digital multimeter [27] and a data acquisition board [28]. Experimental tests were easily carried out using flexible pneumatic tubes with different characteristics in terms of lengths, diameters and fluid medium inside the pneumatic tubing. The main specifications of the differential pressure transmitter used for testing purposes includes: a large number of 32 different measuring ranges, varying between a minimum of 0.125 p.s.i. and a maximum of 3200 p.s.i., easily changed by the user by replacing the sensor's diaphragm; an accuracy of  $\pm 0.5\%$  of F.S., including non-linearity and hysteresis errors; a very low-pressure cavity volume of 0.004 cu in. and a flat bandwidth frequency equal to 80 Hz, sensor plus its conditioning circuit, when the varying pressure source is close-coupled to the sensor port. Fig. 3.8 represents the natural frequency associated with pneumatic tubes with different lengths and two different internal diameter values. For each pneumatic tube diameter tests were carried out using lengths varying between 50 cm and 300 cm, with increments of 50 cm.

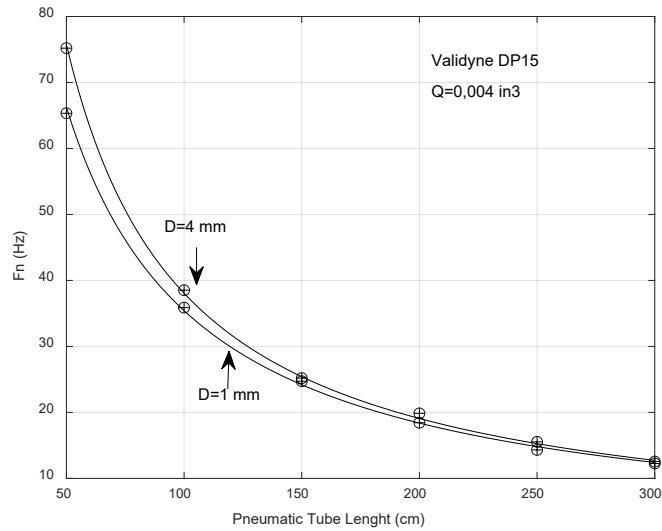


**Fig. 3.8.** Natural frequency of the capillary when its length varies between 50 cm and 300 cm and its internal diameter ( $D$ ) is equal to 1 mm and 4 mm ( $\oplus$  symbol is experimental values; continuous line is theoretical expectations).

As expected from (3.2), the natural frequency imposed by the capillary is inversely proportional to the capillary length being its dependence on capillary diameter very low, since the cavity volume of the PTUD is also very low. By its turn, Fig. 3.9 represents the relative error deviation between experimental values and theoretical expectations for the natural frequency and for the same set of experimental points.

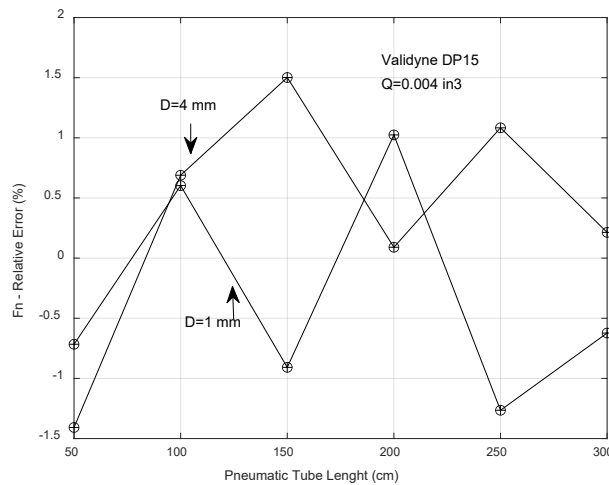


**Fig. 3.9.** Relative error deviation between experimental values and theoretical expectations for the natural frequency of the pneumatic tube when its length varies between 50 cm and 300 cm and its internal diameter ( $D$ ) is equal to 1 mm and 4 mm ( $\oplus$  symbol- experimental values; continuous line- linear interpolation values).

A time response characterization of the pressure measurement channel was also performed using a technique known as pressure step down. Basically, this test was carried out by pressurizing the pneumatic tube to a fixed pressure value, in our case equal to 5 p.s.i., and then the 3-way solenoid valve is actuated and the pressure drops abruptly to the atmospheric value. Fig. 3.10 and Fig. 3.11 represents theoretical and experimental temporal responses for a pressure step down test for two different cases with different damping coefficients that corresponds to an underdamped and overdamped second order system response, respectively.

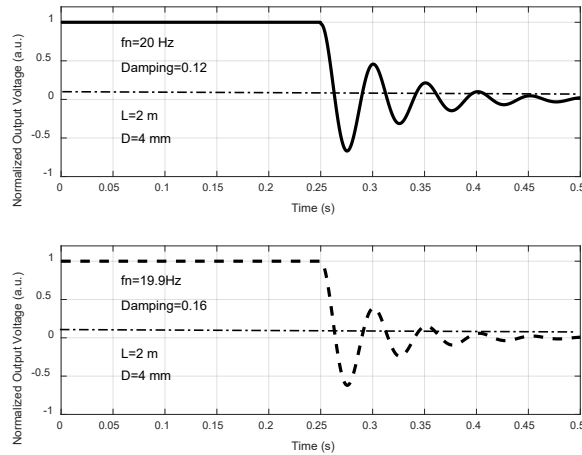


**Fig. 3.10.** Time response of a pressure channel with a pneumatic tube with 2 m length and 4 mm diameter in an underdamped condition (continuous line is a theoretical response; dashed line is an experimental response).

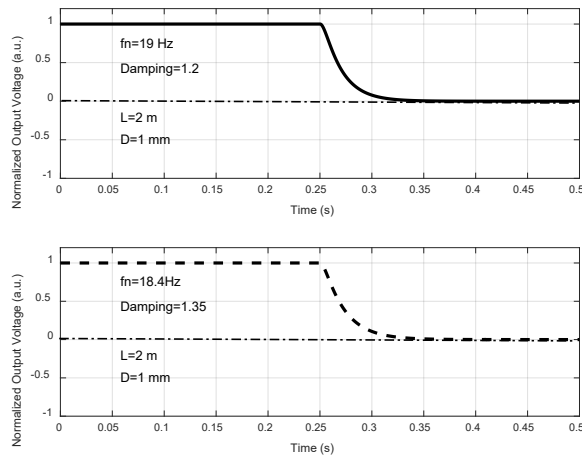


**Fig. 3.11.** Time response of a pressure channel with a pneumatic tube with 2 m length and 1 mm diameter in an overdamped condition (continuous line is a theoretical response; dashed line is an experimental response).

The natural frequencies obtained are a little bit lower than the theoretical expected values. The reason for the difference can easily be justified by the maximum operating speed of the solenoid valve, by the pneumatic tube quality and by the transducer's porting and fittings limitations.

### **3.5.2. Non-invasive Automatic Blood-pressure Sphygmomanometer**

In order to evaluate the performance of the developed prototype with a well-known biomedical device, a comparison between the calibration results that were obtained with our proposed prototype and the results obtained with an accurate biomedical simulator [29], for a given commercial sphygmomanometer [30] was performed. Regarding the sphygmomanometer unit, that was used to compare experimental calibration results, it is important to refer that it is clinically validated in accordance with a large number of certified entities that includes EN 1060 and EN 81060, the European Society of Hypertension (ESH) and the German Association for High Blood Pressure (DHL), among others. The reference simulator is a modular equipment, very versatile and supports maintenance and calibration of NIBP equipment, from the simplest commercial equipment, for home usage, to very accurate equipment used in hospital intensive care units (ICU). The entire system is controlled by an Android™ device, which allows to perform tests remotely. This equipment has large storage capabilities and includes a large number of specific modules that enables the connection of the simulator with the majority of biomedical equipment available in the market. The NIBP module that was used has the following main specifications: NIBP measurement using the oscillometric simulation method; capability to measure the cardiac rate in the range between 20 and 240 beats per minute (BPM) with an accuracy equal to  $\pm 0.25$  BPM; minimum diastolic blood pressure measurement capability of 15 mmHg and a maximum systolic pressure measurement capability of 275 mmHg; regulated pressure source in the range between 10.0 and 400.0 mmHg with an accuracy of  $\pm 0.5$  mmHg and a resolution of 0.1mmHg. Fig. 3.12 represents the test setup that was used to calibrate the home blood pressure monitor.

The blood pressure simulator is configured to periodically generate standardized values for systolic and diastolic pressures with a given rate defined by the desired value of BPM. The pressure signal generated by the simulator is applied to the BP monitor, used for comparative purposes, and to a dummy arm that simulates the human body arm that is surrounded by the sphygmomanometer cuff. In this way, the pressure signal generated by the reference simulator is added with the ramp down pressure signal generated by the BP monitor. As an example, the graph represented in the upper part of Fig. 3.13 represents the pressure signal generated by the simulator and the graph in the down part, of the same figure, represents the associated BP pulses that are superimposed to the pressure ramp signal variations. The configuration defined for the calibration signal is characterized by the following set of parameters: an inflation speed equal to 15 mmHg/s; a deflation speed equal to 5 mmHg/s; and a sampling rate equal to 1024 S/s.

In this experiment the standardized blood pressure signal generated by the simulator is characterized by the following set of parameters: systolic pressure equal to 150 mmHg, diastolic pressure equal to 100 mmHg and a pulse bit rate equal to 60 BPM. After the first

calibration, done with the reference simulator, this simulator was replaced by our calibration prototype using the same configuration parameters that were used with the reference simulator. The set of parametrizations used for a comparative evaluation between the BP prototype and the BP simulator includes the following set of values for BPM, diastolic and systolic pressures: 60-30-40; 80-50-60; 100-65-77; 120-80-93; 150-100-117 and 200-150-167, respectively. Fig. 3.14 and Fig. 3.15 represents the measurement results obtained by the BP monitor.

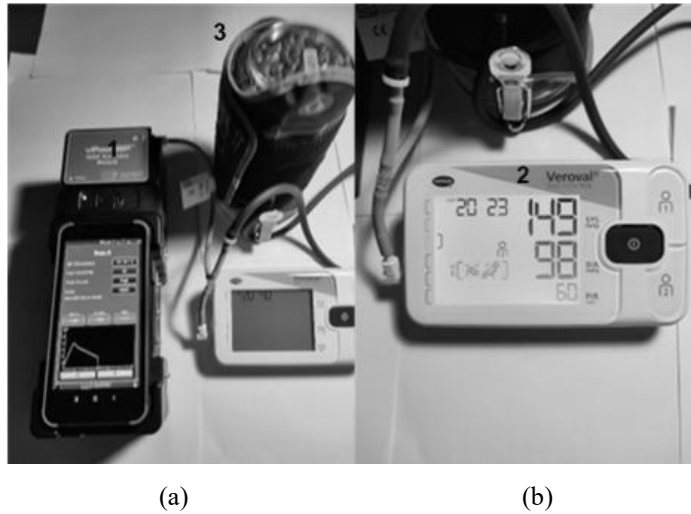


**Fig. 3.12.** Test setup used to calibrate a commercial home blood pressure monitor: (a) equipment interconnections (1 is a biomedical simulator, 2 is a home blood pressure monitor, 3 is a dummy arm used to fix the sphygmomanometer cuff); (b) is a front view of the home blood pressure monitor with displayed results.

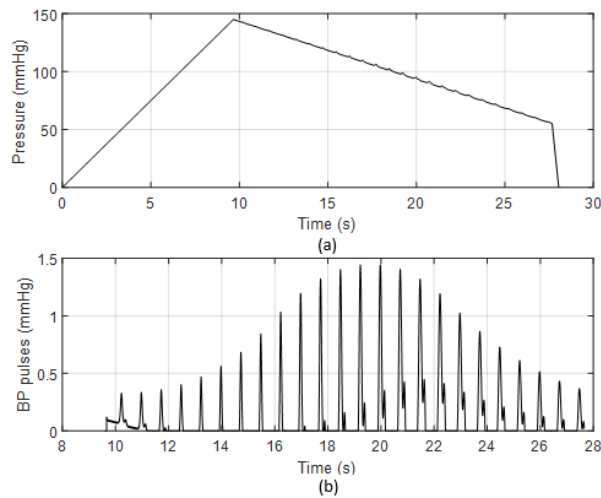


**Fig. 3.13.** Simulator calibration signal: (a) pressure applied to the BP monitor; (b) BP pulses included in the pressure signal.

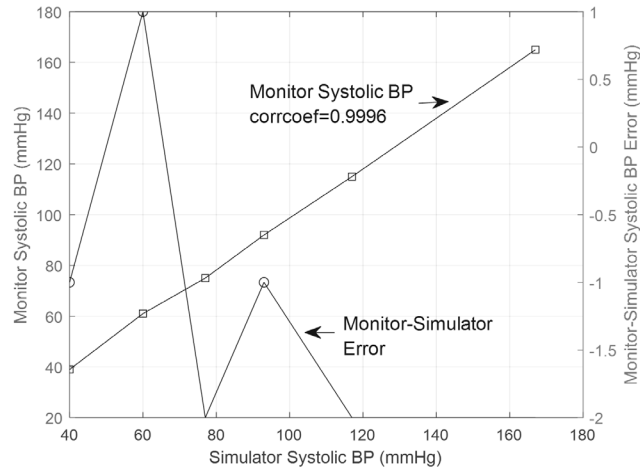


**Fig. 3.14.** Measurement results obtained by the BP monitor using the simulator to perform calibration.

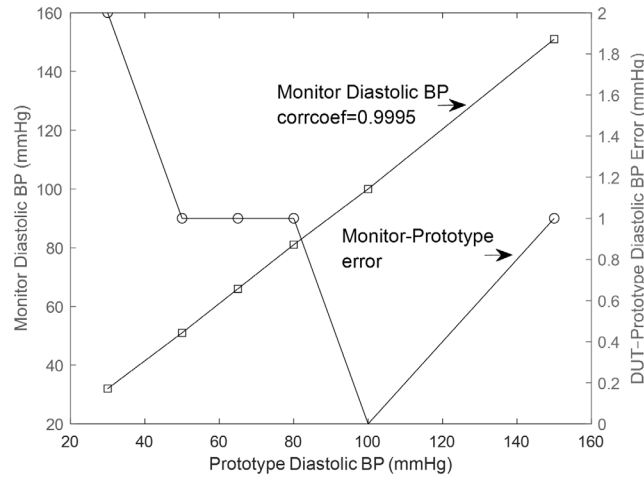


**Fig. 3.15.** Measurement results obtained by the BP monitor using the prototype to perform calibration.

The comparative results obtained with both calibrators, using the same values for systolic and diastolic pressures, are in conformity with the monitor BP measurements and the absolute error, obtained with each one of the calibrators. The absolute error is lower than 2 mmHg, which corresponds to a relative error almost equal to 1.4 % relatively to the pressure measurement range that is equal to 140 mmHg. It is important to refer that this error is lower than the one associated with the technical specification of the BP monitor that is equal to 3 %, being also verified that the maximum BPM relative error is lower than the technical specification value, which is equal to 5 %. Moreover, it is also important to underline that the correlation coefficient values that were obtained, between both calibrators and the BP monitor were better than 0.9995.

### 3.6. Conclusions

This chapter paid a special attention to static and dynamic calibration of pressure measurement channels. Regarding dynamic calibration, it is very important to analyze the frequency response of the different elements that are included in the pressure measurement channel. Whenever the measurement channel includes pressure transmission lines that are frequently used to interconnect pressure sensors to the conditioning circuits of the pressure transmitters, these transmission lines are, usually, the key element that imposes the greatest restrictions in terms of pressure channel bandwidth. In the second part of the chapter a low-cost and flexible calibrator prototype, that can be used to perform static and dynamic pressure calibrations and devices' testing, is presented. The chapter ends with two application examples where dynamic calibration is important. One example is related with the calibration of an industrial pressure transmitter and the other example is related with the calibration of a home blood pressure monitor. In the industrial application example, a particular attention is dedicated to the bandwidth limitations that are associated with the capillaries that are frequently used to interconnect the remote pressure measurement taps to the pressure transmitter. In the second example a comparison, in terms of accuracy, is established between the proposed prototype and a certificated calibrator. As expected, the measurement errors that are obtained with the proposed prototype calibrator are a little bit higher than the errors that are obtained with a certificated biomedical calibrator. However, those results achieved the expected goals, in terms of accuracy, and further improvements are possible to obtain, in a near future, using faster speed 3-way valves and hardware components with better time and frequency performances.

### Acknowledgements

The authors would like to express their sincere gratitude to Instituto Politécnico de Setúbal, ESTSetúbal, Campus do IPS, Estefanilha, Edifício Sede, 2910-761 Setúbal, Portugal, for all received support.

### References

- [1]. V. M. Gusev, N. S. Nesterenko, M. V. Il'ichev, P. A. Konovalov, A. S. Tyuftyaev, Study of coating corrosion resistance for shelf structural objects and oil industry equipment, *Materials Science and Corrosion Protection Chemical and Petroleum Engineering*, Vol. 53, Issue 11-12, March 2018, pp. 745-749.
- [2]. L. H. Cheon, H. Fyhn, A. Hansen, O. Wilhelmsen, S. Sinha, Steady-state two-phase flow of compressible and incompressible fluids in a capillary tube of varying radius, *Transport in Porous Media*, Vol. 147, Issue 1, 2023, pp. 15-33.
- [3]. S. A. Whitmore, Formulation of a General Technique for Predicting Pneumatic Attenuation Errors in Airborne Pressure Sensing Devices, NASA Technical Memorandum 100430, [http://www.nasa.gov/centers/dryden/pdf/88126main\\_H-1462.pdf](http://www.nasa.gov/centers/dryden/pdf/88126main_H-1462.pdf)
- [4]. S. A. Whitmore, W. T. Lindsey, R. E. Curry, et al., Experimental Characterization of the Effects of Pneumatic Tubing on Unsteady Pressure Measurements, NASA Technical Memorandum 4171, [http://www.nasa.gov/centers/dryden/pdf/88178main\\_H-1538.pdf](http://www.nasa.gov/centers/dryden/pdf/88178main_H-1538.pdf)

- [5]. L. Mi, Y. Zhou, Natural frequency analysis of horizontal piping system conveying low viscosity oil-gas-water slug flow, *Process*, Vol. 10, Issue 5, 2022, 992.
- [6]. M. Kovarek et al., Technical Note 1994, Calibration of Dynamic Pressure in a Tubing System and Optimized Design of Tube Configuration: A Numerical and Experimental Study, *National Institute of Standards and Technology*, 2018.
- [7]. Y. Shi, D. Kong, C. Zhang, Research of a sensor used to calculate the dynamic pressure of chemical explosions, *IEEE Sens. J.*, Vol. 21, 2021, pp. 27325-27334.
- [8]. H. Zhuang, Y. Han, H. Sun, X. Liu, Dynamic Well Testing in Petroleum Exploration and Development, *Elsevier BV*, Amsterdam, The Netherlands, 2020.
- [9]. G. Dibelius, G. Minten, Measurement of unsteady pressure fluctuations using capillary tubes, in *Proceedings of the 7<sup>th</sup> Symposium on Measuring Techniques for Transonic and Supersonic Flow in Cascades and Turbomachines*, Aachen, Germany, 1983, pp. 17.1-17.19.
- [10]. J. B. Rosolem, et al., Dynamic effects of temperature on FBG pressure sensors used in combustion engines, *IEEE Sensors Journal*, Vol. 21, Issue 3, 2021, pp. 3020-3027.
- [11]. J. V. Santos de Araújo, J. M. Mauricio Villanueva, M. M. Cordula, et al., Fuzzy control of pressure in a water supply network based on neural network system modeling and IoT measurements, *Sensors*, Vol. 22, 2022, 9130.
- [12]. Q. X. Hu, Y. Yang, W. D. Shi, cavitation simulation of centrifugal pump with different inlet attack angles, *Int. J. Simul. Model.*, Vol. 19, Issue 2, 2020, pp. 279-290.
- [13]. A. Shrivastava, M. Chakkaravarthy, M. A. Shah, A new machine learning method for predicting systolic and diastolic blood pressure using clinical characteristics, *Healthcare Analytics*, Vol. 4, 2023, 100219.
- [14]. S. Taherzadeh, M. Ghasemi, H. Saeedi, et al., Investigation of the effect of ergonomic flooring on the distribution of foot pressure in long standing, *Occupational Medicine Quarterly Journal*, Vol. 13, Issue 2, 2021, pp. 60-67.
- [15]. V. Viegas, J. M. Dias Pereira, O. Postolache, P. Silva Girão, Monitoring walker assistive devices: a novel approach based on load cells and optical distance measurements, *Sensors*, Vol. 18, Issue 2, 2018, pp. 540-545.
- [16]. JCGM-WG2-CD-01, International Vocabulary of Metrology, Fourth Edition, Committee Draft (VIM4 CD), *Joint Committee for Guides in Metrology*, 2021.
- [17]. A. Svete, H. Castro, J. Kutin, Effect of the dynamic response of a side-wall pressure measurement system on determining the pressure step signal in a shock tube using a time-of-flight method, *Sensors*, Vol. 22, Issue 6, 2022, 2103.
- [18]. J. Zakrzewski, K. Wróbel, Dynamic calibration of low range silicon pressure sensors, in *Proceedings of the IEEE Instrumentation and Measurement Technology Conference*, Budapest, Hungary, 2021, pp. 493-496.
- [19]. R. A. Beier, Pressure response of a pneumatic system, *The Technology Interface Journal*, Vol. 9, Issue 2, 2009.
- [20]. I. D. Johnston, Standing waves in air columns: will computers reshape physics courses?, *American Journal of Physics*, Vol. 61, Issue 11, 1993, pp. 996-1004.
- [21]. PCB Piezotronics, Mid-Level Dynamic Pressure Sensor Calibration, Model K9907C, <https://www.modalshop.com/calibration/products/dynamic-pressure-sensor-calibration-systems/medium-range>
- [22]. PCB Piezotronics, High Frequency Dynamic Pressure Sensor Calibration, Model K9901C, <https://www.modalshop.com/calibration/products/dynamic-pressure-sensor-calibration-systems/high-range>
- [23]. Spektra, Piezoresistive Pressure Sensors, Model DPE-01, <https://www.spektra-dresden.com/en/services/dynamic-pressure-calibration.html>
- [24]. Honeywell, Pressure Sensor 24PCBFA6, <https://sps.honeywell.com/us/en/products/advanced-sensing-technologies>



- [25]. Validyne Engineering, DP15 Variable Reluctance Pressure Sensor Capable of Range Changes, [https://www.validyne.com/product/dp15\\_variable\\_reluctance\\_pressure\\_sensor\\_capable\\_of\\_range\\_changes/](https://www.validyne.com/product/dp15_variable_reluctance_pressure_sensor_capable_of_range_changes/)
- [26]. Tameson, 1/8" 3-Way 24V DC Electric Solenoid Valve, <https://tameson.com/products>
- [27]. Digital Multimeter, Model 34405A, [https://ecelabs.njit.edu/student\\_resources/34405-91000%20Digital%20Multimeter.pdf](https://ecelabs.njit.edu/student_resources/34405-91000%20Digital%20Multimeter.pdf)
- [28]. National Instruments, Multifunction DAQ, USB 6210, <https://www.ni.com/pt-pt/shop/model/usb-6210.html>
- [29]. DATREND Systems, Vpad-BP NIBP Simulator, <https://www.qrs-solutions.com/products/datrend-systems-vpad-bp>
- [30]. Paul Hartmann AG, Veroval DUO CONTROL, <https://www.veroval.info/en-ae/technology>

# Sensors, Measurements and Sensor Systems

**Sergey Y. Yurish, Editor**

*Sensors, Measurements and Sensor Systems* (Volume 9 of the *Advances in Sensors Book Series*) presents cutting-edge research at the forefront of sensor design, calibration techniques, and advanced measurement systems. This volume continues the series' mission of highlighting rigorous, high-impact work from international experts across academic and engineering communities.

The book brings together multidisciplinary insights that span the theoretical foundations and practical implementations of modern sensing technologies. Emphasis is placed on methodological innovation, system integration, and experimental validation — making it a relevant and timely resource for researchers tackling complex real-world measurement challenges.

This volume is intended for a scholarly audience, including PhD students, and research professionals in electrical engineering, applied physics, instrumentation, and related fields. Its content is particularly suitable for postgraduate coursework, and as a reference for dissertation research or laboratory development.



ISBN 978-84-09-57646-3

